Passive Mechanical Heat/Mass Exchange Enhancement by Semi-Confined Laminar Parallel Wall Jets

F.-J. Granados-Ortiz*, J. Ortega-Casanova
Fluid Mechanics, Universidad de Málaga, Andalucía Tech
C/ Dr Ortiz Ramos s/n, 29071 Málaga, Spain
*Corresponding author: fjgranados@uma.es

Abstract

Many different approaches have been investigated in the literature to achieve efficient heat and mass exchangers in applications in several fields such as mechanical, aeronautical or biomedical engineering. Some of these engineering devices need to efficiently mix two fluids at different temperature or concentrations, achieving a decent mixing at a low power cost, and using passive mechanical elements if possible. This paper introduces and analyses numerically the novel application of two parallel wall jets to enhance mixing by vortex shedding induced mechanically. The numerical approach is the non-uniform finite difference approximation, used for the first time in the study of mixing mechanics. The parallel wall jets are constrained within a channel, which can be a simple and passive easily manufactured machine with high potential as scalable laminar mixing device. Different wall jet geometries and Reynolds numbers have been tested with a verified&validated CFD code based on non-uniform finite difference approximation. This analysis allowed to predict configurations that lead to unsteady oscillatory motion. In general, it has been observed that for a range of laminar wall jets, a small channel ratio seems a very efficient option for heat/mass transfer, thanks to the intense oscillation generated in the flow downstream, which enhances mixing with low power requirement.

Keywords: CFD, heat transfer, mass transfer, mixing machines, mechanical engineering

Accepted manuscript in IJMS - DOI: 10.1016/j.ijmecsci.2021.106623 *January 27, 2025*

Nomenclature

Roman Symbols

$\langle - \rangle$	Time-averaged value.
$\vec{v}$	Velocity vector.
C	Solute concentration/Temperature.
C_0	Characteristic solute concentration/temperature.
D	Thermal diffusivity/molecular diffusivity.
f	Oscillation frequency.
g	Arbitrary magnitude.
H	Channel width.
h	Wall jet width.
h'	Distance from the channel wall to the opposite wall jet.
L	Channel total length.
mec	Mixing energy cost.
Nx	Total number of nodes in the x direction.
Ny	Total number of nodes in the y direction.
ny_1	Number of nodes along the wall jet width in the y direction.
ny_2	Number of nodes along the zone between wall jets in the y direction.
p	Pressure.
Pe	Peclet-like number.
q	2D channel flow rate.
q_j	2D wall jet flow rate.
Re	Reynolds number.
St	Strouhal number.
t	Time.
t_0	Reference time.
U	Channel inlet mean velocity.
u,v	Velocity components.
U_j	Jet inlet mean velocity.
VS	Vortex shedding.
Y	Dimensionless mixing quantity.
x,y,z	Cartesian coordinates.

Abbreviations

ADE	Alternating Direction Explicit.
ADI	Alternating Direction Implicit.
CFL	Courant-Friedrich-Lewy number.
GCI	Grid Convergence Index.

Subscripts

max	Maximum value.
pp	Peak-to-peak value.
t	Partial derivative in time t.
x, xx	First and second partial derivatives in x.
$x = a$	$x = a$ location.
$xx0$	Finite difference approximation of the second derivative in x with null first derivative.
y, yy	First and second partial derivatives in y.
$yy0$	Finite difference approximation of the second derivative in y with null first derivative.
i,j	Nodal location.

Greek Symbols

Δ	Magnitude difference.
η	Mixing efficiency [%].
μ	Dynamic viscosity.
∇^2	Laplace operator.
ω	Vorticity component in z coordinate.
Π	Pumping power.
ψ	Dimensionless streamfunction.
ρ	Density.
σ	Standard deviation.
$\vec{\Omega}$	Vorticity vector.
$\vec{\Psi}$	Potential vector.

Superscripts

in	Position at the inlet.
n	Iteration number.
$wall$	Wall surface position
$\hat{—}$	Dimensional magnitude (SI units).

1. Introduction

Heat and mass transfer is a frequent requirement in applications such as heat exchangers [1] and combustion engines [2] in mechanical engineering, aircraft and rocket jets [3] in aeronautical engineering, chemical synthesis [4] in chemical engineering, or microfluid-based Lab-On-Chip devices for disease diagnosis [5] in biomedical engineering, amongst many others. In these engineering applications, fluid mixing may play a critical role, which generates considerable interest in achieving high mixing efficiency [1]. The mixing efficiency term η is one of the most important aspects in the present manuscript, since this parameter is a measure of how well fluids are mixed. A perfect mix ($\eta = 100\%$) at the outlet means that the mixing device achieved the maximum efficiency.

Traditionally, researchers have classified devices for mixing of fluids into a passive and active devices [6]. Active devices include moving elements that enhance mixing, and can actually deploy a wider range of control options by varying the frequency of motion of an active element. However, they have the drawbacks of requiring additional power consumption, increase complexity in the design, and require maintenance. Additionally, if the device is intended at microscale, the deployment of tiny stepwise motors may not be feasible. All these inconveniences are not present in passive devices. For these, usually obstacles are aggregated to the channels to promote mixing at zero cost (except when drag forces must be overcome thus increasing pumping power). In terms of scaling up, the use of passive devices is attractive at reduced scale because of the said drawbacks in active devices. Thus, a good advantage of the passive mixer is that fluid mechanics will work similarly even if scaled-up from micro to macroscale. Nevertheless, at nanoscale the present continuum mechanics will not be applicable and mixing mechanics may not respect the present results [7]. Although the mixing device can be scaled-up from micro to macroscale in terms of fluid mechanics, the specific application will also play an important role on the overall performance. There are certain disciplines where efficient scale-up may not be easy, such as industrial production

of biodiesel [8], because of larger channel sections influence axial dispersion of bulk phase components and methanol phase; polymer manufacturing [9], as a result of scaling-up of involved chemical reactions as well; or carbon fiber manufacturing [10], due to high costs attributed to gas mixing and release in manufacturing furnaces.

In terms of design of a passive mixing machine, the most popular application is to use different channel shapes (T-shaped, F-shaped, zig-zag, etc.) or to place objects at the walls as mixing promoters. In [11] a T-shaped channel was used to mix two fluids at different temperature and low Reynolds. In [12] F-shaped units were used to enhance mixing, yielding improved mixing with respect to the T-shaped channel. In [13], Y-shaped and complex shaped channels were tested numerically and experimentally for mixing, achieving an important enhancement in mixing. An important limitation in "shaped" mixers (T-shaped, F-shaped, etc.) is that the pumping power cost is highly increased in comparison to straight channels [14, 15]. As said, to place objects in the channels is another way to enhance mixing. Examples of this approach can be found extensively in the literature. For instance, in [16] two bars were placed as mixing unit in a microchannel to enhance low-Reynolds mixing. An optimisation study was carried out to find the best angles for the bars to decrease the pumping power and maximise mixing. Similarly, Tayeb et al. [17] tested square-shaped protuberances in a zig-zag fashion to promote mixing between two shear-thining non-Newtonian fluids. In addition, other chaotic shapes were tested to achieve more energetically efficient mixing. Tseng et al. [18] also tested the combination of diamond-shaped pillars with adjacent square-shaped protuberances for laminar mixing. They used such configuration to promote vorticity and generate secondary flows in spanwise planes. Although to promote mixing by using objects or obstacles is interesting, it suffers from increasing pumping power if the placement of elements slowdown the flow notably, as observed in the aforesaid investigations.

Another efficient option to enhance mixing by a passive method is to use vortex shedding. One of the side effects of this approach is that the detached vortical structures have the capability to enhance mixing if the object is placed suitably. Examples of

success can be found in [1, 19], where a rectangular pillar is placed in the centreline of a microchannel. Since two inlet laminar flows at different temperature/mass fraction are entering the microchannel, the centreline also coincides with their separation in the inlet and the pillar object is placed to split both flows. Due to the collision with the pillar, above a critical Reynolds number (which is fully dependent on the geometry of the channel, pillar and flow regime), vortex shedding structures appear and these promote thermal/molecular mixing between the two flows. This phenomenon is important and can be actually predicted by means of Machine Learning methods on this geometries, as done in [20]. Despite geometries of short aspect ratio pillars have been studied in the literature as said, the impact of very large aspect ratios leading to vortex shedding for mixing has not been investigated. When the aspect ratio is as long as the flow can be fully developed on top and bottom of the pillar object, this situation can be also interpreted as the mixing between two parallel fully-developed channel flows discharging into a large channel, or two laminar wall jet mixing. Due to the geometry and flow regime conditions, the flow is detached at the end of the split channels, and may lead to vortex shedding structures.

Although the investigation on vortex shedding mechanics has been in continuous development since a century ago, this is still a topic of high interest nowadays. There are many researchers that investigated recently relevant characteristics of the mechanics of the oscillatory motion of detached flows. For instance [21] developed an experimental work on vortex shedding at subcritical regime using Particle Image Velocimetry (PIV) and pressure surface measurements. In such research was observed that the early separation of flow led to larger downstream wakes. Important modes of oscillation were identified as well, with Proper Orthogonal Decomposition techniques (POD) on the pressure fluctuation data, which explained the most relevant vortex shedding characteristics. Some authors also tested the effect on vortex shedding due to the aggregation of fins and other elements, as in [22]. In this work was tested experimentally the effect on vortex shedding of adding fins to a circular cylinder, observing certain control on the recirculation behind the body. Other authors in the literature, as e.g. [23] studied

laminar flows passing through arrays of elements, to predict the transitional behaviour of the flow as a function of the density of object pins. In this work was studied how the density of pins can control the transition to unsteady flows, since relations between the critical Reynolds number and the Roshko number with the density of pins were found. For heat transfer enhancement, in [24] the laminar flow-induced vibration of a D-section cylinder confined in a channel is studied numerically. An oscillatory motion of the downstream flow takes place due to the intensification promoted by the galloping motion of the object, enhancing heat transfer notably but under complexity due to the moving object. A very similar problem was also studied in [25], but oriented to harvest the energy from the dynamic combination of vortex-induced vibration and galloping motion.

Confined vortex shedding is an example of application where ground effects are important in the characteristic flow mechanics. Several researchers have investigated the effect of ground or walls on the development of the vortical structures. For instance in [26] an oscillatory flow detached from a flat plate was analysed numerically. This work demonstrated that the spacing between the flat plate and the ground wall highly affects the detached flow. As the gap between the flat plate and the ground was decreased, the strength of the vortex shedding was decreased, which is consistent with experimental data. An interesting experimental study on confined vortex shedding was developed in [27], where the shape of objects, effect of blockage ratio and Reynolds number was assessed. The analysis concluded that the size of the spacing between the walls and the object was the most influential aspect, which was able to activate/deactivate the unsteady oscillatory mechanics of the flow. In [1, 28] vortex shedding past a confined square cylinder was promoted and boosted to enhance mixing between two fluids, similarly to the objective in the present manuscript. The oscillatory motion was found very influenced (and predictible [20]) by proper combination between the blockage ratio, aspect ratio and Reynolds number. More comments on the relevant effect of the blockage ratio and other geometric parameters in the behaviour of the downstream confined flows can be found in other recent works in the literature [29, 30, 31, 32]. This activation of

confined vortex shedding is the objective of the present work to enhance mixing.

To the knowledge of the authors, there is no literature on the use of laminar wall jets for thermal/mass mixing enhancement. Laminar mixing is specially difficult, since there is no turbulence aiding the mixing process as in other heat/mass applications with turbulent jets [33, 34]. The motivation to study a laminar mixing device instead of a turbulent mixing is that some applications do not deal with flows at enough speed to involve turbulence. A good example is the biomedical engineering field. For instance, when the fluid to be mixed is blood, turbulence is avoided as much as possible. Turbulence in blood can lead to important complications for the pathophysiology of the vascular system, including mechanical hemolysis (destruction of red blood cells, releasing their content into the blood stream flow) [35]. Another application is the administration of vaccines. Some vaccines such as Pfizer-BioNTech COVID-19 Vaccine requires mechanical mixing with a diluent by a trained nurse [36]. This process is carried out manually by inverting the recipient twenty times (10+10). This must be done gently to avoid shaking [37], thus this process can be done efficiently by a mechanical mixer using wall jets. As the flow is not impinging on objects or obstacles, the wall jet mixing device is a novel recommendation for nearly any sensitive laminar fluid . The only work found that considered a wall jet configuration is [38], who developed a single simulation of a wall jet (their work was more focused on twin jets), not extracting any feedback on design modifications. In their work, two laminar twin jets in a semi-confined space were simulated in a 2D computational domain. They tested different positions of the twin jets, until they achieved a wall jet case scenario. They found out that the best mixing with ambient flow took place for the wall jet, what encouraged the present work.

Apart from [38], the most related studies to this topic in the literature are those that investigate mixing/instabilities between twin free/semi-confined jets, but these do not evaluate heat or mass transfer. However, Nahum and Seifert [39] suggested years ago the use of twin jets as mixing improvement in micromixing applications and studied numerically and experimentally in detail confined twin jet instabilities, as well

as the use of harmonic excitation to enhance mixing. In [40] the self-oscillatory motion of confined turbulent twin jets from round and squared cross sections was analysed in detail numerically. In this study it was observed that if the spacing between jets is not large (lower than four times the diameter), the two jets merge downstream and behave like a single oscillatory jet. Such oscillation is due to the formation of vortical structures suffering expansion, elongation, and contraction. When the spacing is increased, the jets oscillate individually. However, it is interesting the observation that when the spacing is increased, the oscillation frequency is not significantly affected. Oscillatory characteristics of dual jets were also analysed in [41], where an experimental study on two jets are entering into a dome-shape mixing chamber was developed. The oscillatory motion was controlled mainly by the flow rate and complex vorticity patterns are observed inside the mixing dome. Some studies on turbulent jet mixing such as [42] just consider a wall jet in tandem with a free jet (parallel offset jet), thus the mixing is not constrained to a channel geometry. In their study they studied experimentally both jets at $Re = 10^4$ and found vortex shedding-like structures in the shear layer interaction similar to those detached from a bluff body; opposite to the free jet only scenario in which Kelvin-Helmholtz instabilities dominate along the shear layer. In [43] the interaction of a wall jet and an offset jet is also studied but numerically. In their work they varied gradually the ratio of the mean velocity of these jets and studied different turbulence models. Another investigation on the interaction between an offset jet and a wall jet can be found in [44]. In this work, the interaction of these jets is analysed numerically, and they observed again a very strong impact of the offset ratio on the development of the flow structures. There are also few applications of confined (or semi-confined) twin jets. In [45], 2D simulations of three laminar twin jets in a semi-confined channel were developed. Jet mixing is studied focused on the critical Reynolds above which the problem becomes transient and thus mixing is enhanced. The author concluded that for the three-jet device the flow could be stable&symmetric (with low Reynolds), unstable&symmetric (with moderate Reynolds), and unstable&asymmetric (with high Reynolds). Recently, some authors also tested the use of confined jets in

thermal mixing. For instance, in [46] two turbulent parallel confined jets at different temperature are passing thorough perforated obstacles (porous surfaces) at a certain distance to study numerically and experimentally the influence on thermal mixing. They observed that despite the obstacles have a positive impact on mixing, turbulence is reduced downstream. A very similar and recent work was developed in [47], where the authors tested the improvement in thermal mixing of confined turbulent twin jets by placing cylindrical obstacles at a certain distance. The mixing efficiency was improved with this method by testing numerically and experimentally the use of different row of obstacles. In [48], Artificial Neural Networks (ANN) are trained with experimental data from the thermal mixing between two turbulent twin jets in a cross-section narrow channel. In this work several design parameters were taken into account (jet inclination, temperature difference, jet flow ratio, jet diameters), which once input to the ANN model, the thermal output can be predicted.

All the aforementioned works strongly motivated the application of parallel wall jet flows in a channel for our thermal/mass transfer applications, since the interesting interaction between the shear layers of both flows is worthy of investigation. The most important novelty in the present work is that we aim to design a novel laminar wall jet mixer, by testing geometric and flow regime variations, with a special interest in boosting vortex shedding to enhance mixing. Since this design is oriented to improve the state-of-the-art in scalable micromixing, we also pay attention to obtain a device with low pumping power and high mixing efficiency.

Regarding the numerical code used in this work, the non-uniform finite difference approach [49] has been successfully applied to other previous works in the literature, such as sudden expansions [50] or vertical pipe flow instability analysis [51]. However, the method has not been applied to thermal or molecular mixing of flows before. The most popular approach in the literature of mixing is the use of finite volume [1] or finite element methods [52]. With respect to the use of non-uniform grids in general CFD applications, some authors have developed recently hybrid approaches such as the hybrid finite difference-finite volume schemes [53], which benefits of the higher

order convergence property of finite difference methods and the conservativeness of finite volume methods when applied on a non-uniform mesh. Nevertheless, this method is useful only if there is an abrupt change in the flow, since for areas of uniformity, the computational costs are unnecessarily increased. In [54] the use of a high-order unconditionally stable Alternating Direction Explicit (ADE) scheme is proposed to solve the stability and efficiency problems on non-uniform grids that takes place in the standard ADE scheme. This method allows to solve the fluid diffusion equation on non-uniform grids by means of a fourth-order finite difference approximation, achieving important reduction in elapsed time of computations. The method has been applied in [55]. The present work uses a similar approach to ADE, which is the Alternating Direction Implicit (ADI) scheme [50]. Thus, to use a non-uniform finite difference approach provides some advantages, such as the possibility to implement an in-house numerical code, which is simpler to code than finite element/volume methods, and has the advantages of saving computational resources as a consequence of the adaptive non-uniform meshes. The use of finite difference is also advantageous for this specific geometry, since the domain is fully rectangular so the grid is rectangular as well and the method is very efficient in solving the governing partial differential equations. The use of a non-unform nodal distribution also provides the advantage of avoiding the use of immersed boundary conditions, in addition to the advantages in stability, accuracy and simplicity of using a Cartesian grids [49]. For complex domains, finite element or finite volume methods are usually preferred over finite difference schemes, as their integral formulation does not have a priori any mesh structure preference [56]. In the present investigation it is demonstrated that the in-house code is a useful approach to evaluate and analyse thermal/molecular mixing of flows. In addition, whilst the use of commercial softwares is acceptable in many scenarios, CFD practitioners do often write their own codes in order to include or develop new approaches or modules. Moreover, there are strong limitations in commercial softwares to deploy intrusive features such as, for instance, optimisation methods or intrusive uncertainty quantification methods [57, 58].

The paper is divided into the following sections. Section 2 introduces the geometry of the mixing device, as well as the governing equations and the numerical approach carried out, which includes also validation of numerical results. Section 3 is dedicated to the discussion of the results. Finally, Section 4 summarises the conclusions from this investigation.

2. Governing Equations and Numerical Approach

The geometry under study is shown in Fig. 1. It consist of a 2D channel with two incompressible fluids which comes in from the left side. A mass flow rate $\hat{q}_j$ of a fluid 1, with a solute concentration (or a temperature, if the application is heat transfer) of value $\hat{C}_0$, comes into the channel through its lower half. Additionally, another and identical mass flow rate $\hat{q}_j$ of a fluid 2, which is solute free (or it has a different temperature if heat transfer is considered), enters through the upper half of the channel. Both fluids have the same density $\hat{\rho}$ and viscosity $\hat{\mu}$. If mass transfer is considered, this assumption is correct. However, for heat transfer, since density and viscosity is temperature dependent, this would be only correct if the temperature difference between fluids 1 and 2 does not lead to sensitive differences between the properties of these flows. The channel is $\hat{H}$ meters wide, $\hat{L}$ meters long, and has a solid separation between inlets, so that $\hat{h}$ is the wall jet width. Defining $\hat{U}_j$ as the mean upper and bottom inlet velocities, the mass flow rates $\hat{q}_j$ can be written as

$$\hat{q}_j = \hat{U}_j \hat{h}, \tag{1}$$

so the total mass flow rate through the channel is

$$\hat{q}_j + \hat{q}_j = 2\hat{q}_j = \hat{q} = \hat{U}\hat{H}, \tag{2}$$

where U is the mean velocity at the channel exit.

Defining the dimensionless parameters $L \equiv \hat{L}/\hat{H}$ and $h \equiv \hat{h}/\hat{H}$, we have then for the velocities $\hat{U}_j = \frac{\hat{q}_j}{\hat{h}} = \frac{\hat{U}\hat{H}}{2\hat{h}} = \frac{\hat{U}}{2h}$. We shall also define the dimensionless distance $h' \equiv 1 - h$, which is the distance from the channel lower side to the pillar upper one.

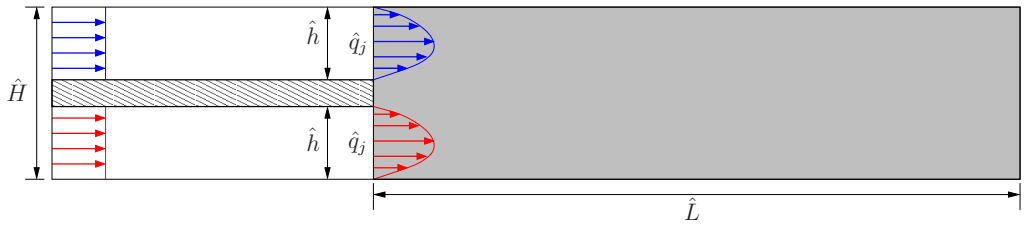

Figure 1: Sketch of the geometry of the two parallel wall jets (represented by blue and red velocity profiles). The area shadowed in gray is the computational domain.

In this study, both wall jets are fully developed Hagen-Poiseuille flows. This assumption allows to reduce the computational domain to a rectangular region downstream the inlets, i.e. the shaded region of Fig. 1, with perfectly identified boundary conditions for the two jets that enter the computational domain above and below the pillar, as shown in Fig. 1.

By using as characteristic magnitudes $\hat{U}$, $\hat{H}$ and $\hat{H}/\hat{U}$ to make dimensionless velocity, length and time, respectively (in Cartesian coordinates (x, y, z)), the stream function-vorticity $(\psi - \omega)$ formulation [59, 60] will be used to solve the 2D incompressible flow on the (x, y) plane. Firstly, the velocity components are related to the stream function as:

$$\vec{v} = (u, v, 0) = \nabla \wedge \vec{\Psi} = \nabla \wedge (0, 0, \psi) = (\psi_y, \ -\psi_x, 0), \tag{3}$$

where the subscripts x and y denote the partial derivatives in x and y, respectively. Secondly, by means of the definition of the vorticity $\vec{\Omega}$ one has

$$\vec{\Omega} = \nabla \wedge \vec{v} = (0, 0, v_x - u_y) = (0, 0, \omega). \tag{4}$$

Thirdly, by combining both equations, one can obtain

$$-\omega = \psi_{xx} + \psi_{yy}, \tag{5}$$

where the double subscript means second order partial derivative. Finally, from the z-coordinate of the transport equation of the vorticity $\vec{\Omega}$, it yields

$$\omega_t + \psi_y \omega_x - \psi_x \omega_y = \frac{\omega_{xx} + \omega_{yy}}{Re}, \tag{6}$$

where Re is the Reynolds number $Re = \dfrac{\hat{\rho}\hat{U}\hat{H}}{\hat{\mu}}$ (which can be also written as $Re = \dfrac{\hat{\rho}2\hat{U}_j\hat{h}}{\hat{\mu}}$ to make it based on jet characteristics), and all subscripts denote partial derivatives. Equations (5) and (6) are a system to solve both components of the velocity but not the pressure field, since it does not appear in the mathematical formulation of the problem. The corresponding boundary conditions to solve Equations (5)–(6) are described in Appendix A.

Both fluids, which enter into the channel through the left hand side, will be mixed downstream. If $\hat{C}$ is defined as the solute concentration of the fluid in any position, by using $\hat{C}_0$ to make $\hat{C}$ dimensionless, one can then define $Y = \hat{C}/\hat{C}_0$, which is called dimensionless mixing quantity in this work. This quantity would be the dimensionless mass fraction of the fluid in a mass transfer problem, or dimensionless temperature in a heat transfer application with two fluids at different temperature. Since the most important quantity of interest is the mixing efficiency, in order to know how the dimensionless scalar magnitude Y evolves along the channel the convection-diffusion equation governing the process can be written as [61, 62]:

$$Y_t + \psi_y Y_x - \psi_x Y_y = \frac{Y_{zz} + Y_{yy}}{Pe}, \tag{7}$$

where $Pe = \dfrac{\hat{U}\hat{H}}{\hat{D}} \left(= \dfrac{2\hat{U}_j\hat{h}}{\hat{D}} \right)$ is the Peclet-like number, with $\hat{D}$ the molecular diffusivity (in mass transfer) or thermal diffusivity (in heat transfer). The corresponding boundary contidions to solve Equation (7) are described in Appendix B.

As aforesaid, the pressure field is not explicitly solved in the mathematical formulation. If one is interested in solving also the dimensionless pressure field p once ψ, w and Y are known, then the corresponding Poisson equation for p (derived from the divergence of the momentum equation) must be solved. In terms of primitive variables, this is [63, 64]:

$$\nabla^2 p = -2(v_x u_y - u_x v_y), \tag{8}$$

whilst in terms of ψ, it can be written as

$$\nabla^2 p = 2(\psi_{xx}\psi_{yy} - \psi_{xy}^2). \tag{9}$$

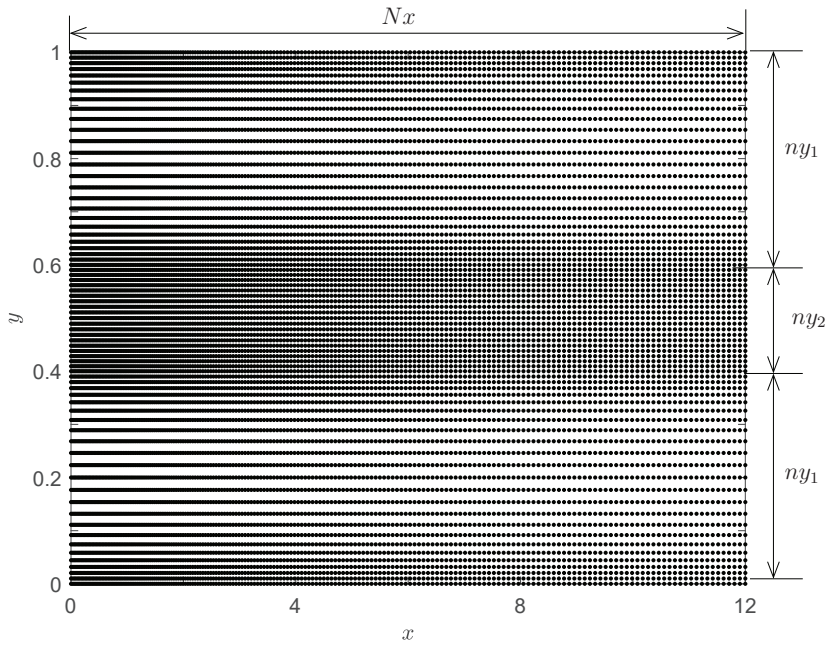

Figure 2: Nodal distribution with $Nx = 200$, $Ny = 70$ ($ny_1 = 25$, $ny_2 = 20$) for $L = 12$ and $h = 0.4$. The nodes are clustered in the central part of the microchannel, as this is the main mixing contact area. There is also more compression in the walls, to properly solve the boundary layer.

The corresponding boundary conditions to solve Equation (9) are described in Appendix C.

The oscillatory behaviour of any magnitude, say g, at the channel outlet because of the development of a downstream oscillatory flow (which will depend on Re and h), will be characterised by its frequency of oscillation $\hat{f}$. This frequency is represented in dimensionless notation by means of the Strouhal number: $St = \hat{f}\hat{H}/\hat{U}$. In this case, its time-averaged value during an oscillation period St^{-1} can be computed as

$$\langle g \rangle = \frac{1}{St^{-1}} \int_{t_0}^{t_0+St^{-1}} g(t')\, dt', \tag{10}$$

being t_0 any dimensionless time reference for the periodic flow.

Pressure losses are an important aspect in flows through pipes or channels. This parameter defines the pumping power required for the fluid to flow along the duct. Concretely, this is the power needed to maintain a given flow rate $\hat{q}$ along the channel, for which the pressure and viscous losses must be overcome (which can be evaluated as the inlet-outlet pressure difference times the mass flow rate). Thence, the dimensionless

pumping power, denoted by Π, can be evaluated as

$$\Pi = \frac{\langle \Delta \hat{p} \rangle \, \hat{q}}{\hat{\rho} \hat{U}^3 \hat{H}}, \tag{11}$$

where $\Delta \hat{p}$ is the dimensional pressure drop between the channel inlet and outlet. Due to the chosen characteristic magnitudes, finally the pumping power can be written as

$$\Pi = \frac{\langle \Delta \hat{p} \rangle}{\hat{\rho} \hat{U}^2} = \langle \Delta p \rangle, \tag{12}$$

which means that the inlet pumping power is governed by the dimensionless pressure drop along the channel.

Finally, the most important parameter in the design of the device is the assessment of the mixing quality at the channel outlet. This feature is defined as the mixing efficiency η, in %. According to previous works (e.g. [65, 62, 1]), this quantity of interest can be written as:

$$\eta = \left(1 - \frac{\langle \sigma \rangle}{\sigma_{max}} \right) \times 100, \tag{13}$$

where σ is the standard deviation of the corresponding scalar magnitude at the channel exit, and σ_{max} is the maximum standard deviation at the inlet (which is a 0.5 in the present two fluids mixing problem). Due to the fact that $0 \leq Y \leq 1$, then $0 \leq \sigma \leq 0.5$, where $\sigma = 0$ means uniform distribution of Y at the outlet with full mixing ($\eta = 100\%$); whereas $\sigma = 0.5$ would mean a very poor mixing ($\eta = 0\%$). Due to the fact that the efficiency η can be evaluated at any longitudinal location x and not just only at the outlet, the subscript $x = a$, with a being the corresponding coordinate, in $\eta_{x=a}$ indicates the location where the efficiency is evaluated, unless evaluated at the outlet (no subscript). This will allow us to assess how the channel performs, i.e. how the efficiency increases, from a till the outlet. This shows the benefits of increasing the length of the channel. To that end, the efficiency difference will be defined as

$$\Delta \eta = \eta - \eta_{x=a}. \tag{14}$$

Another important parameter to assess the goodness of each mixing device is the relation between the required pumping power and the mixing efficiency. This is the

so-called mixing energy cost mec, which is defined as [66]

$$mec = \frac{\Pi}{\eta}. \tag{15}$$

This quantity is a measure of the required energy per each percentage unit of mixing achieved.

The present work is focused on the investigation of different configurations of wall jets to enhance mixing thanks to vortex shedding mechanics. In order to clearly differentiate the impact of geometry from other contributions such as variations in the fluid properties, phases, etc., the complexity of the problem in terms of cross-effect contributions has been kept simple. This does not mean at all that more complex applications are unfeasible. Actually, these are encouraged.

In terms of fluid properties, the present study is extensible to any viscosity and density fluid. Moreover, if the fluid is non-Newtonian, viscosity can be input as a function easily. Must be recall that if density and viscosity do change, these parameters are part of the Reynolds number definition. Therefore, if the Reynolds and Peclet-like numbers are constant, the outcome does not change. The Reynolds number also involves flow velocity. Thus, as long as compressible effects are not present (e.g. shocks at high-speed), any velocity profile and magnitude can be imposed at the inlet. Temperature is another interesting parameter. The present study considers either an isolated heat transfer problem or mass transfer problem, in order to facilitate the understanding of the impact of the wall jet geometry in mixing. Including cross-effects would affect mixing, thus wrong conclusions may be extracted. For instance, when studying mass transfer, locations of high/low temperature would vary molecular diffusivity, and the impact of wall jets on mixing may not be that clear. Finally, multiphase simulation is also another interesting possibility for problems involving more than one phase. The present investigation is a single-phase simulation, but for multiphase problems the numerical approach would still be valid. Unfortunately, computational resources would be more demanding: for multiphase modelling one should select and code a specific modelling: Eulerian model, Volume of Fluid (VOF) model, etc. Although this can be

implemented onto the present code, this would not be straightforward. For a successful implementation of the streamfunction-vorticity formulation in a multiphase flow, see for instance [67]. As final conclusion, it is remarked that all the discussed features can be combined at once into the simulation, in order to predict the performance of more complex mixing applications using wall jets. The only "limitation" that one may encounter in the customisation of the simulation is the imposition of inlet pressure. Unfortunately, the streamfunction-vorticity formulation does not allow to impose pressure boundary conditions. The pressure field is solved at a final stage once the velocity field is obtained and the pressure at inlet is adapted to the one needed to get the corresponding flow.

2.1. Numerical Details

A non-uniform mesh [49] with mesh nodes clustered close to the inlets and side walls has been used. The transient set of Equations (5)-(7) has been solved by means of finite difference-based numerical scheme [49], where central second order spatial finite difference approximations have been used for spatial partial derivatives. Regarding the temporal terms of the equations, these have been discretised with a central first order scheme. Therefore, if Equation (6) (and similarly Equation (7)), is discretised in an arbitrary mesh node (i, j) and time instant n, it is obtained:

$$\omega_t|_{i,j}^n + \psi_y|_{i,j}^n \omega_x|_{i,j}^n - \psi_x \omega_y|_{i,j}^n = \frac{\omega_{xx}|_{i,j}^n + \omega_{yy}|_{i,j}^n}{Re}, \tag{16}$$

from which the explicit equation for the interior unknowns $w|_{i,\,j}^{n+1}$ can be obtained by

$$\omega|_{i,j}^{n+1} = \omega|_{i,j}^n + \Delta t \left(NLT|_{i,j}^n + VIS|_{i,j}^n \right), \tag{17}$$

where NLT and VIS stand for the discretisation of the Non Lineal Terms and Viscous ones, respectively. Starting from an initial solution ψ^0, ω^0 and Y^0 (the whole domain is initialised with $Y^0 = 0$, as well as $\psi^0 = \psi^{in}$ and $\omega^0 = \omega^{in}$, whose values are defined in Appendix A), Equation (17) (and the equivalent for Y) allows to advance in time ω (and Y) from $n = 0$ to $n = 1$. After that, the discretisation of Equation (5) with second order spatial finite difference approximations in $|_{i,j}^{n+1}$ is

$$\psi_{xx}|_{i,j}^{n+1} + \psi_{yy}|_{i,j}^{n+1} = -\omega|_{i,j}^{n+1}. \tag{18}$$

This allows, by solving the corresponding highly sparse set of equations, to solve the unknowns of ψ at each interior node. Then, the boundary conditions are updated at the next time step by means of the expressions given in Equations (A.2)–(A.5). This three-step scheme consists of knowing: i) ω^{n+1} and Y^{n+1} on the interior points; ii) ψ^{n+1} on the interior points; and iii) ω^{n+1}, ψ^{n+1} and Y^{n+1} on the boundaries. Such scheme is repeated iteratively until the flow reaches a steady or periodic (oscillatory) behaviour.

2.2. Validation

To validate the abovementioned methodology, three 2D problems with analytical solutions and a fourth comparison with data from literature have been solved. The first validation test case aims to check if the fully developed 2D Poiseuille flow is kept along a straight channel when this solution is used as initial condition, as it is depicted in Fig. 3(a). A parabolic x-velocity profile with null y-velocity

$$\vec{v} = (u, 0, 0) = (6y(1-y), 0, 0), \tag{19}$$

is imposed onto the inlet of the geometry by means of ψ and w as

$$\psi = 6(y^2/2 - y^3/3),\ w = 6(1-2y). \tag{20}$$

The results at the outlet, in terms of both primitive and non-primitive variables, are shown in Fig. 4. The absolute error with respect to the theoretical profile is also shown. As can be seen, the agreement with the expected solution is very good. Additionally, the solution given by the Poisson pressure in Equation (9) has been compared with the theoretical pressure drop $\Delta p = 12L/Re$. This comparison is shown in Fig. 4(e), where a very good agreement can be observed for the range of Reynolds numbers under study.

The second validation test case is dedicated to check the development of the parabolic Poiseuille x-velocity profile from a uniform profile. To that end, the geometry and boundary conditions shown in Fig. 3(b) are numerically simulated. In the figure is depicted that there is a very short piece of channel upstream (end marked with two black points at the channel walls) with constant uniform x-velocity $u = 1$. This is so

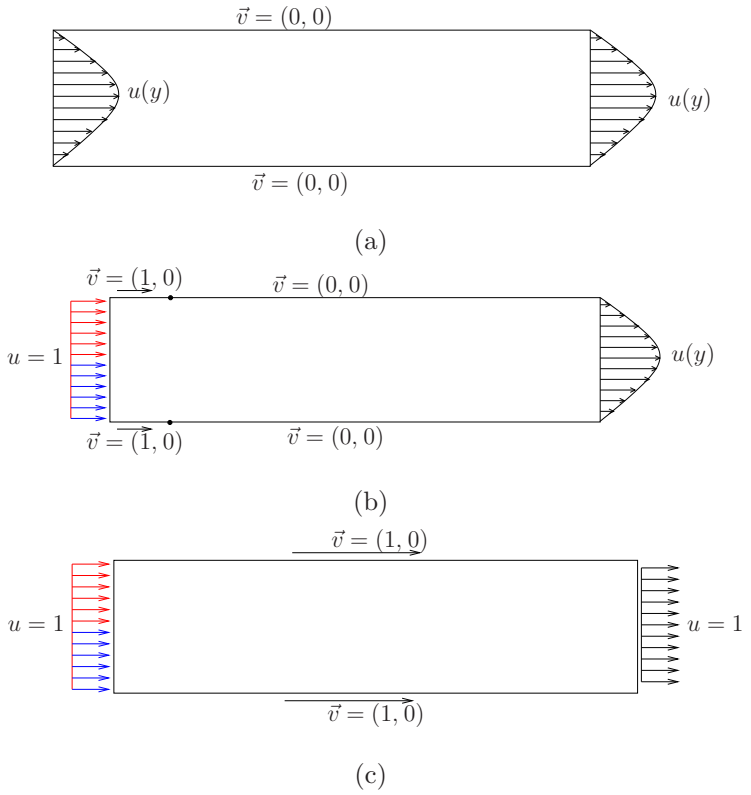

Figure 3: Sketch of the geometries and boundary conditions used in the validation step. Parabolic and uniform axial inlet profiles have been simulated: (a) 2D Poiseuille flow under constant pressure gradient; (b) Development of a 2D Poiseuille flow; (c) Convection-diffusion of a scalar magnitude in a uniform flow with translational moving walls in the axial direction.

because this facilitates to the flow to adapt to the computational domain. The size of the small portion of the channel with imposed uniform velocity is for the fluid to progressively adapt to the no-slip wall. If the length L of the channel is long enough, a fully developed Poiseuille flow will exit the channel at the outlet, as can be seen in Fig. 5, where the streamlines and vorticity contour are plotted for the two channel lengths used. Fig. 5(c)-(d) show that close to the exit, the streamlines and vorticity contours are almost horizontal, which evidences that a fully developed flow has been reached. This, however, does not happen in the shorter channel in Fig. 5(a)-(b). This can be validated by comparing the fluid properties at the outlet with the theoretical/fully developed ones. This is shown in Fig. 6, where the primitives and non-primitives variables at the outlet are compared. One can see that the the longer the channel, the better the

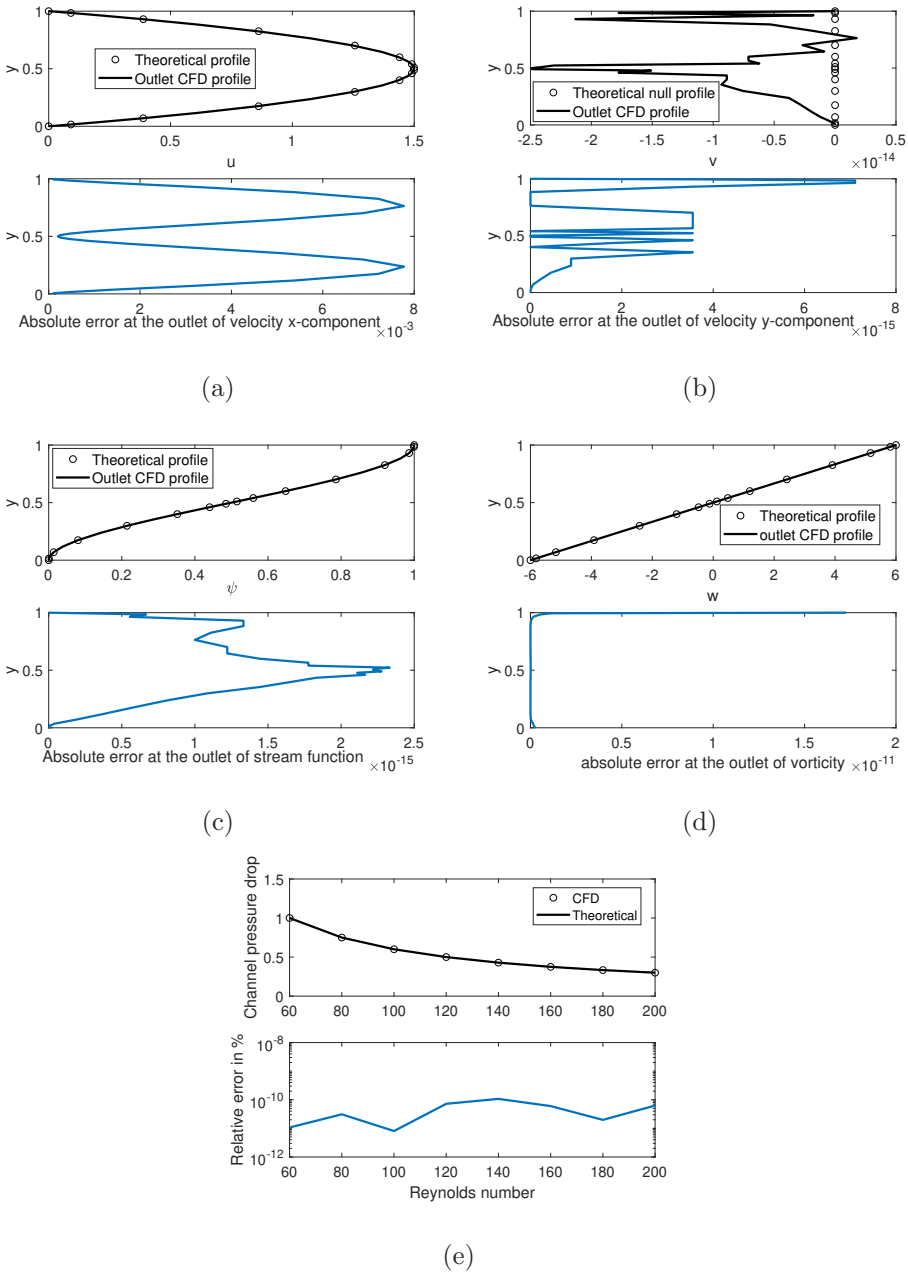

Figure 4: Validation of CFD simulations with theoretical data: (a) and (b) validation by means of primitive variables; (c) and (d) by means of non-primitive variables; (e) validation of computational channel pressure drop. In each subfigure the top plots correspond to the validation, and the bottom plots are the numerical absolute error. The markers correspond to theoretical data and the solid lines are numerical results.

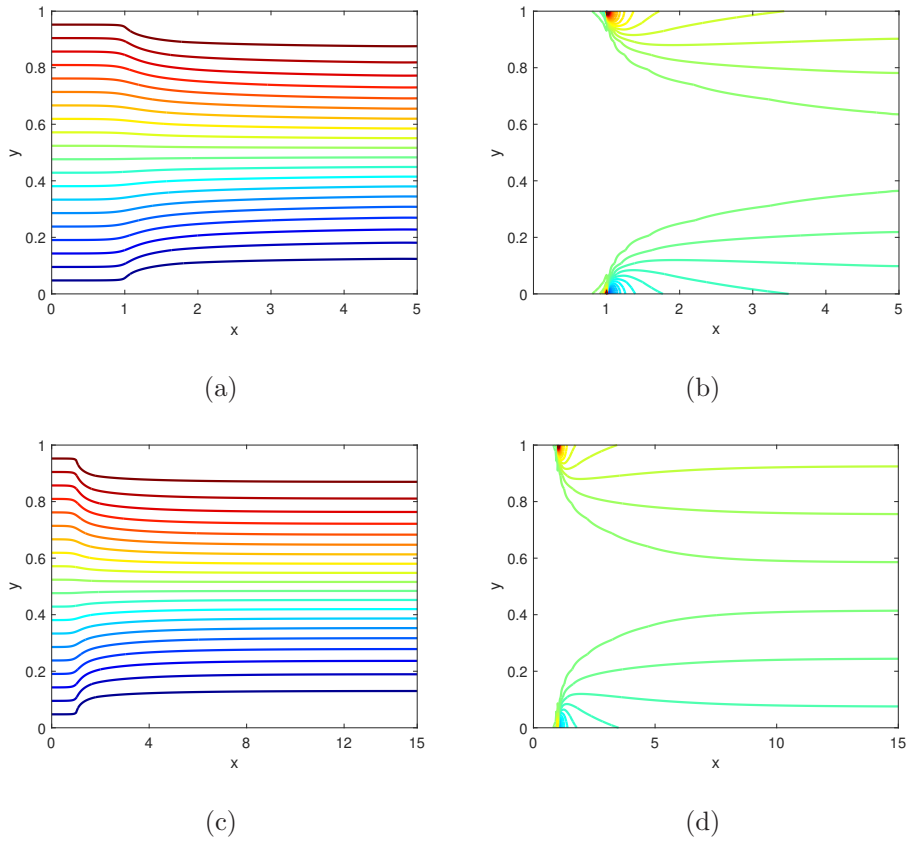

Figure 5: Non-primitive variables contours for the second validation test and two different channel lengths: (a)-(b) for $L = 5$; and (c)-(d) for $L = 15$. (a) and (c) are streamlines, and (b) and (d) isolines of vorticity ω. It can be observed that the initial uniform profile is transformed into a parabolic profile as the flow develops. The initial uniform flow is kept until $x = 1$ due to a small portion of pipe is artificially modelled as moving at the same velocity to facilitate the adaption of the flow. The area of highest vorticity takes place around $x = 1$ also for this reason.

agreement with the theoretical profiles.

The third validation test case is dedicated to validate the computational approach when the convection-diffusion equation is solved coupled with the flow motion. To that end, the problem shown in Fig. 3(c) is studied: a uniform flow enters a channel where both side walls are moving at the same velocity too. Under these conditions, the solution at any point of the domain in terms of primitive variables is $\vec{v} = (1, 0, 0)$.

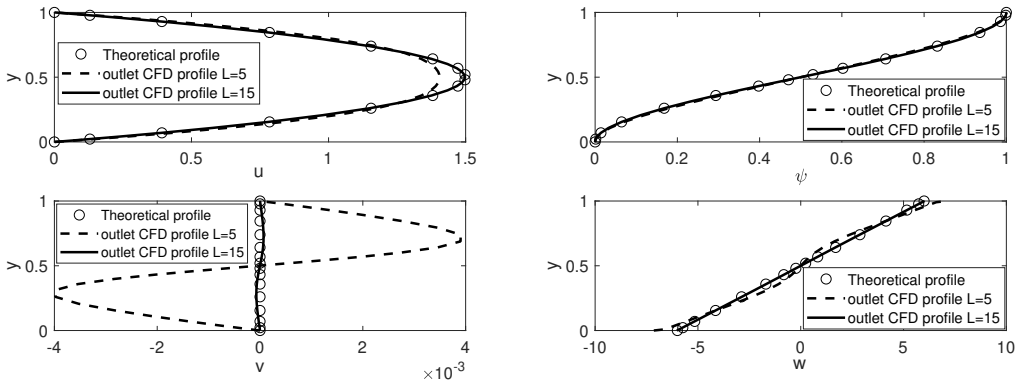

(a) (b)

Figure 6: Comparison of the (fully developed) velocity profiles at the outlet for the second validation test and the different channel lengths: (a) for primitive variables; and (b) for non-primitive variables. The marker data corresponds to theoretical data, and the solid lines are numerical data. As the channel length is increased, the discrepancy between the theoretical fully developed flow data and numerical data is reduced as expected.

Taking this into account in Equation (7), the steady state simplifies to

$$0 = \frac{Y_{zz} + Y_{yy}}{Pe}. \tag{21}$$

With the boundary conditions in Equations (B.2)-(B.5), Equation (21) can be solved by separation of variables, obtaining [61]:

$$Y(x,y) = \frac{2}{\pi}\sum_{k=1}^{\infty} \frac{\sin(k\alpha\pi)}{k} \cos(k\pi y) \exp\left(-\frac{2k^2\pi^2}{Pe + \sqrt{Pe^2 + 4k^2\pi^2}}x\right) + \gamma \tag{22}$$

where $\gamma = q_1/(q_1 + q_2)$ is the ratio of the upper half flow rate to the total one. For U = constant and $\gamma = 0.5$, the comparison of the CFD solution and Equation (22) is shown in Fig. 7, where x and y profiles of Y are compared for two Peclet-like numbers. As shown, the agreement is excellent.

Finally, a fourth validation test case is run with the CFD code. The simulation corresponds to the streamlines of a wall jet problem studied in Rafferty and Kaminski [38], likewise validated with three different sources from the literature. The configuration of the geometry (according to the notation used in the present paper) is $h = 0.05$

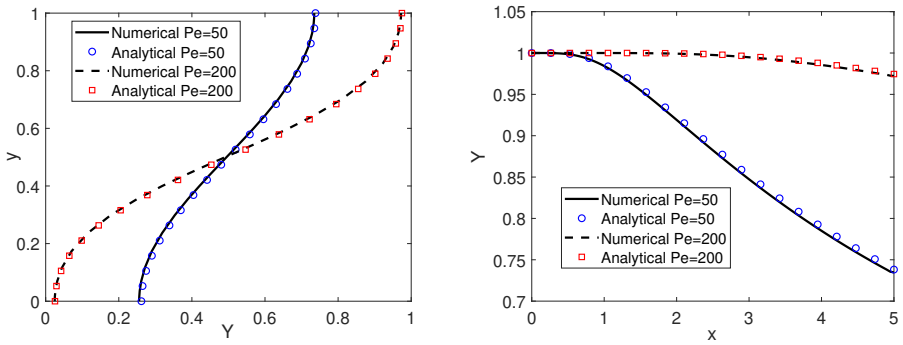

(a) (b)

Figure 7: Comparison between numerical and analytical solutions of Y for the indicated Peclet-like numbers at different x and y positions: (a) profiles along y coordinate at $x = 5$; and (b) profiles along x coordinate at $y = 1$.

and channel length $L = 30/4$. The Reynolds number under study, according with our definition, is $Re = 70$, and the inlet velocity of the jets are uniform velocity profile. The comparison between our numerical results and those reported in Rafferty and Kaminski [38] is shown in Fig. 8. The results show almost no difference between each figure, concluding with this tested case the validation of the numerical procedure.

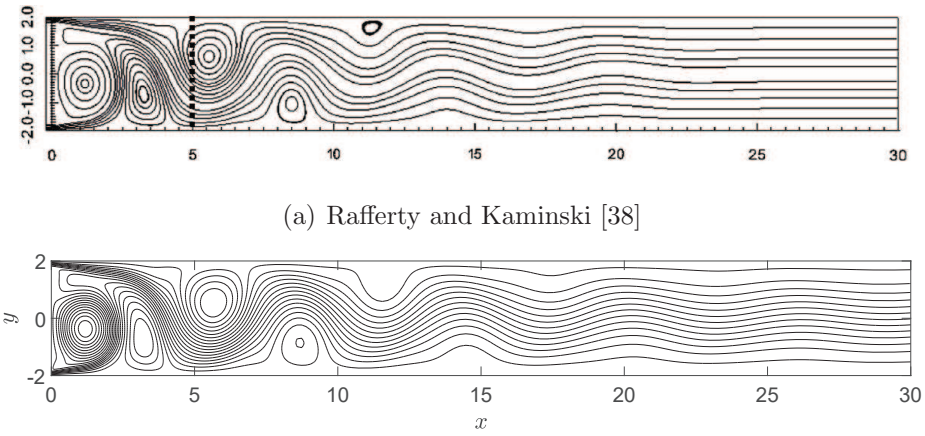

(a) Rafferty and Kaminski [38]

(b) Current CFD simulation

Figure 8: Validation of streamlines with data reported in Rafferty and Kaminski [38] (subfigure (a) reproduced with permission). Subfigure (b) is the current numerical simulation of the streamlines.

2.3. Grid Convergence Study

Instead of using a generic and unique mesh for all geometric configurations under study, a detailed grid convergence study has been carried out for the three different values of h of this study: $h = (0.1, 0.2, 0.4)$. Thanks to the Grid Convergence Index GCI [68], an optimal number of nodes has been identified for ny_1, ny_2 and Nx (see Fig. 2). Regarding the input parameters, the most unfavourable situation with $Re = 200$ and $Pe = 200$ has been analysed. This provides a robust measure of confidence on the optimal mesh. Once the geometric configuration is selected, at least three values are given for the number of nodes in a specific region, while the other two remains constant, in order to find an adequate number of nodes that allows to perform the simulation at higher accuracy but lower computational cost. The magnitude analysed during the GCI procedure was the mixing efficiency η at the outlet.

To start with, the top and bottom inlet mesh with $h = 0.4$ will be analysed first. Initially, with fixed values of $ny_2 = 20$ and $Nx = 240$, three values of $ny_1 = (20,\ 25,\ 30)$ have been simulated. These corresponds to a total number of nodes in the y-direction of $Ny = (60, 70, 80)$. In next figures, the inverse of the total number of nodes on the coordinate direction on which the sensitivity is being analysed, will be used for the x-axis to see the convergence of the solution. The corresponding mixing efficiency together with the error bars given by the GCI procedure is provided in Fig. 9(a). The grid with $ny_1 = 25$ nodes gives an acceptable discretisation error of 3.5%, thus is chosen as the optimal one. Once ny_1 is fixed to 25, different values of ny_2 are tested. The number of nodes in the x direction is fixed to $Nx = 240$ again. The ny_2 has been ranged as $ny_2 = (15, 20, 15)$, which corresponds to $Ny = (65, 70, 75)$. The mesh with $ny_2 = 20$ yields a discretisation error of 3.9%, so this is chosen as the optimal one (see Fig. 9(b)). Finally, the value for Nx is ranged between $Nx = (220, 240, 260, 280)$, whilst ny_1 and ny_2 are fixed to the said optimal values. As can be seen in Fig. 9(c), the effect of the different grids on the efficiency is quite low, and an intermediate value of $Nx = 240$ is finally chosen. Therefore, for $h = 0.4$ the optimal grid selected is $(ny_1, ny_2, Nx) = (25, 20, 240)$, which means a total of $Ny \times Nx = 70 \times 240$ nodes.

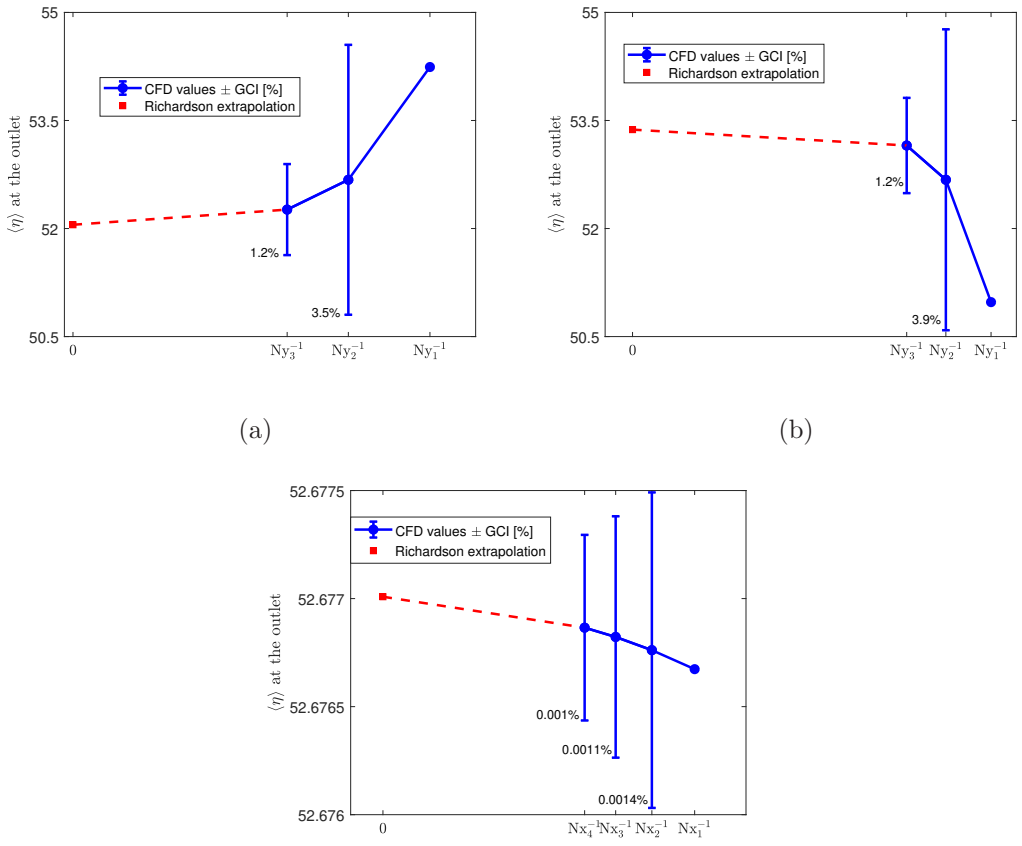

Figure 9: Grid convergence study to select the number of nodes for: (a) ny_1; (b) ny_2; and (c) Nx. $h = 0.4$, $Re = 200$, $Pe = 200$. The blue dots are the CFD values obtained for each mesh, whereas the error bars are the discretisation error (Grid Convergence Index) due to the refinement. The red dashed line is the expected value of $\langle\eta\rangle$ towards the Richardson extrapolated value (red square marker).

Regarding the inlet of medium size, $h = 0.2$, the GCI study was initiallised with fixed values of $ny_1 = 15$ and $Nx = 240$, and three values of $ny_2 = (30, 40, 50)$, corresponding to $Ny = (60, 70, 80)$. The corresponding mixing efficiency together with the error bars given by the GCI procedure are shown in Fig. 10(a). The grid with $ny_2 = 40$ nodes gives an acceptable discretisation error of 1.4%, and is chosen as the optimal option. Next, three different values of ny_1 are simulated with fixed $Nx = 240$: $ny_1 = (16, 21, 26)$, which corresponds to $Ny = (72, 82, 92)$. The mesh with $ny_2 = 21$ yields a discretisation error of 3.3%, so this is accepted as optimal option, see Fig. 10(b). Finally, the value

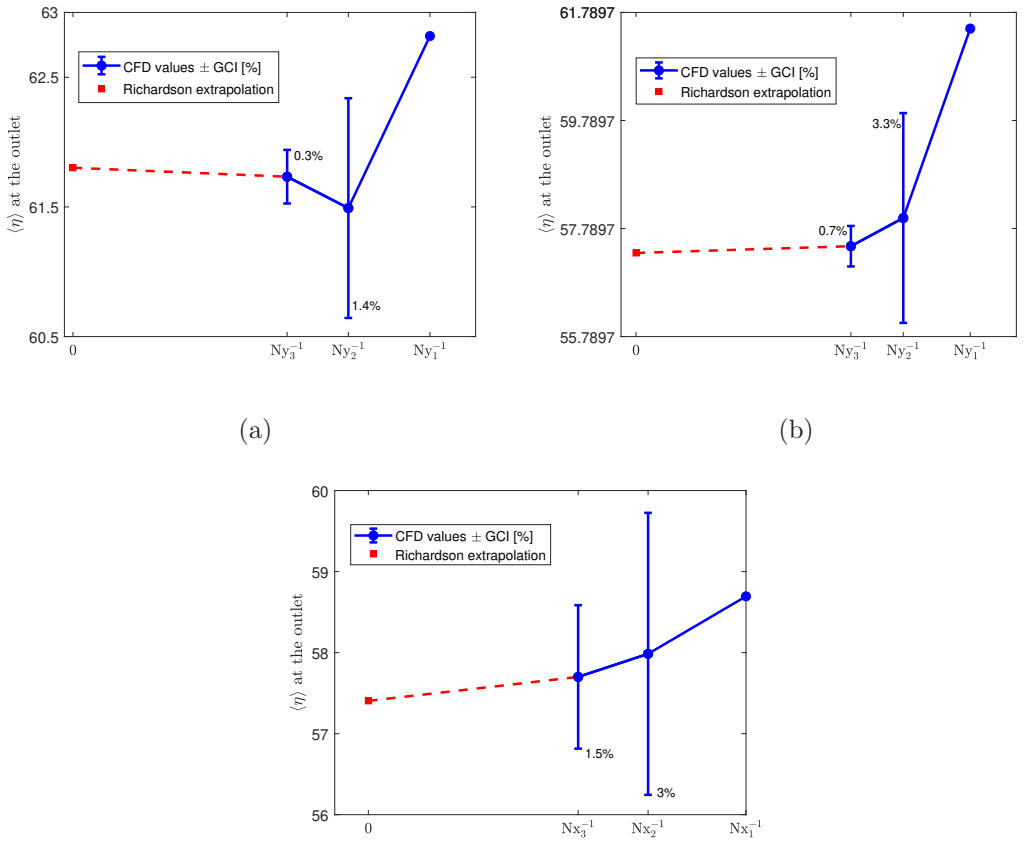

Figure 10: Grid convergence study to select the number of nodes for: (a) ny_1; (b) ny_2; and (c) Nx. $h = 0.2$, $Re = 200$, $Pe = 200$. The blue dots are the CFD values obtained for each mesh, whereas the error bars are the discretisation error (Grid Convergence Index) due to the refinement. The red dashed line is the expected value of $\langle\eta\rangle$ towards the Richardson extrapolated value (red square marker).

for Nx is selected from $Nx = (200, 240, 280)$, whereas ny_1 and ny_2 are the fixed optimal values. The medium mesh with an acceptable error of around 1.5% is selected as the optimal one (see Fig. 10(c)), which corresponds to $Nx = 240$. Therefore, for $h = 0.2$ the optimal grid is $(ny_1, ny_2, Nx) = (21, 40, 240)$, which means a total of $Ny \times Nx = 82 \times 240$ nodes.

Finally, for $h = 0.1$, the GCI was conducted for ny_1 with $Nx = 200$ and $ny_2 = 80$. The values of ny_1 simulated were ranged as $ny_1 = (10, 15, 20)$, corresponding to $Ny = (100, 110, 120)$. As can be observed in Fig. 11(a), the medium value of

$ny_1 = 15$ nodes gives a very acceptable discretisation error of 0.05%. Next, three values of ny_2 were tested: $ny_2 = (40, 60, 80)$, with $ny_1 = 15$ and $Nx = 200$ as fixed values. This scenario corresponds to $Ny = (70, 90, 110)$. In this case, given that the solid wall between both inlets is the highest ($0.8H$), the finest grid with $ny_2 = 80$ with a discretisation error of 0.1% was selected (see Fig. 11(b)). To conclude the GCI analysis, the value of nx was ranged as $Nx = (180, 220, 260)$. The medium mesh with $Nx = 220$ nodes with a discretisation error of 2.3% was finally selected as the optimal option, whose performance can be seen in Fig. 11(c). Therefore, for $h = 0.1$, the optimal grid has $(ny_1, ny_2, Nx) = (15, 80, 220)$ as nodal distribution, which means a total of $Ny \times Nx = 110 \times 220$ nodes.

Regarding the time integration, the stability of the explicit scheme to advance in time the transport Equations (6) and (7) was assured by choosing a time step for the Courant-Friedrich-Lewis number to be much lower than unity. This has been done so for the most unfavourable configuration ($Re = 200$ and $Pe = 200$) on each geometric configuration. This dimensionless number for every cell i,j, based on the magnitude velocity $|\vec{v}_{i,j}|$ and the grid cell diagonal, is evaluated as

$$CFL = \frac{\Delta t \sqrt{|\vec{v}_{i,j}|}}{\sqrt{\Delta x_{i,j}^2 + \Delta y_{i,j}^2}}. \tag{23}$$

Once the time step is chosen in order to keep $CFL < 1$ $\forall i,j$, it is fixed for the other Reynolds and Peclet-like numbers. In particular, for $h = 0.1$ the highest Courant was around 0.3; for $h = 0.2$, the maximum was around 0.1; and for $h = 0.4$, it was around 0.025. In all configurations, these maximum values appear close to the inlets, where the velocities are the highest and the grid cells the smallest.

3. Results

The performance of the parallel wall jets for laminar mixing purposes can be assessed from different viewpoints. Although the mixing efficiency can be improved by, for instance, the aggregation of obstacles or the increase in the length of the channel, this

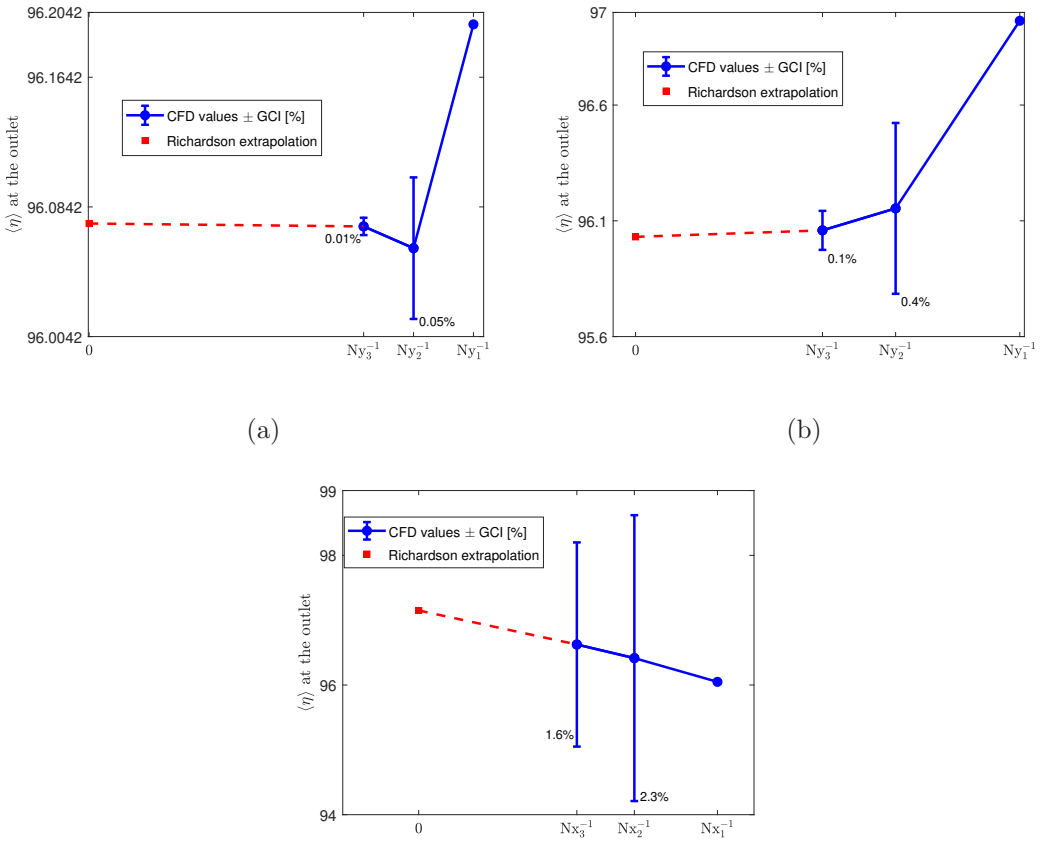

Figure 11: Grid convergence study to select the number of nodes for: (a) ny_1; (b) ny_2; and (c) Nx. $h = 0.1$, $Re = 200$, $Pe = 200$. The blue dots are the CFD values obtained for each mesh, whereas the error bars are the discretisation error (Grid Convergence Index) due to the refinement. The red dashed line is the expected value of $\langle\eta\rangle$ towards the Richardson extrapolated value (red square marker).

would lead to an increase in pressure drop too. The higher the pressure drop, the less efficient the mixing machine would be, since a high pumping power requirement may be not practical for certain applications. It is hence expected a high mixing efficiency at a low pumping power need. For the objective to analyse in detail the performance of the mixing machines at different working conditions and geometrical configurations, in this section will be analysed the effect on mixing efficiency, pressure drop (and mixing energy cost) and the effect of the length of the channel.

3.1. Effect on Mixing Efficiency

In terms of mixing performance, it has been observed how the Reynolds number Re, Peclet-like number Pe, and dimensionless blockage ratio (wall jet width) h affect the mixing efficiency. As expected, the lower the h, the more efficient the mixing is, since the jets have more time to grow separately before they are in contact. This leads to a very decent mixing even without vortex shedding, and specially remarkable for low Pe, due to the molecular/thermal diffusion effects. Diffusion is dominant in flows with low viscosity (low Peclet-like, i.e. high Schmidt number for molecular diffusion or high Prandtl number for thermal diffusion). This performance is shown in Fig. 12.

It can be observed in Fig. 12 that when Pe is increased, the mixing efficiency is greater for smaller values of h. This effect is not strictly due to the Pe itself, but the geometry. That is, the behaviour of the flow across the channel is highly affected by the dimensionless blockage, leading to configurations with and without downstream oscillations. This performance is summarised in Fig. 13, where the micromixer configurations that lead to oscillatory structures are represented by circles. At the background, contours of the peak-to-peak value of η (η_{pp}) are plotted. These contours represent the amplitude of the oscillation of η. As aforesaid in fluids with high Pe, $h = 0.4$ geometries yielded lower mixing efficiency than $h = 0.1$ and $h = 0.2$. The reason is that for those geometries with $h < 0.4$, the oscillatory downstream flow enhances mixing, opposite to $h = 0.4$, which has barely oscillation (see Fig. 13 and the colorbar scale). It can be actually seen that in Fig. 12(a), $Re = 60$ is less efficient than higher Reynolds because that configuration did not present an oscillatory flow in Fig. 13(a). Likewise, one can extract the same conclusions between Figs. 12(b) and 13(b).

Whilst one expects a high η_{pp} for configurations leading to high η, the situation is actually the opposite upon comparison between Figs. 12 and 13. This is because diffusivity (mixing by diffusion) is more dominant than mechanical mixing (vortex mixing) in this type of problem. This is evidenced in the high Pe case, which has less dominancy of diffusion. In this scenario, the higher values of Pe lead to high values of η_{pp}, which correspond to high values of η.

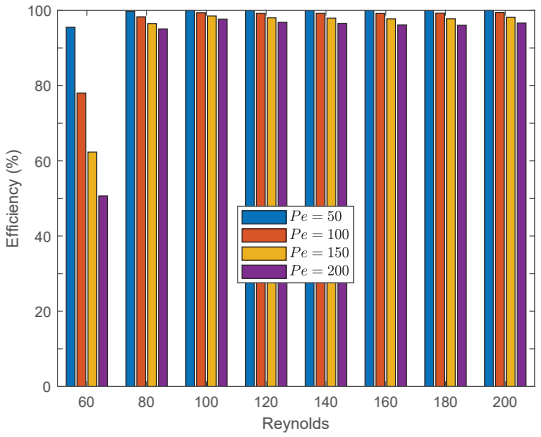

(a) $h = 0.1$

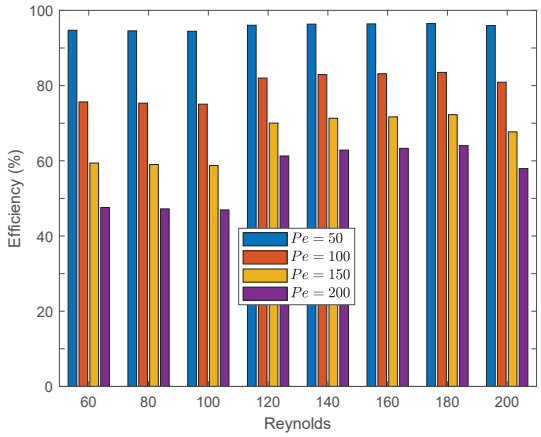

(b) $h = 0.2$

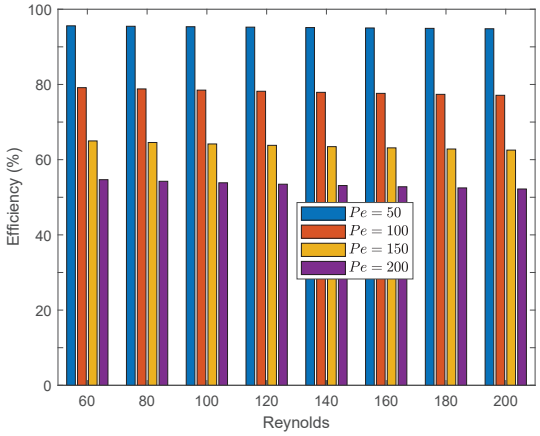

(c) $h = 0.4$

Figure 12: Efficiency as function of Re and Pe for different configurations of the jets: (a) $h = 0.1$; (b) $h = 0.2$; and (c) $h = 0.4$.

The more intense the oscillatory motion of the vortex streets, the better the mixing. The oscillations appearing for each configuration can be observed in Figs. 14-16. As discussed before for the Reynolds numbers considered in this work, configurations with low h values tend to exhibit more intense oscillations. Configurations with $h = 0.4$ exhibit no oscillation, and mixing is entirely attributed to thermal/molecular diffusion. This makes important to know beforehand whether a configuration may or may not lead to downstream oscillations. There are previous works in the literature on the prediction of this of behavior by means of Machine Learning models in flows around objects to

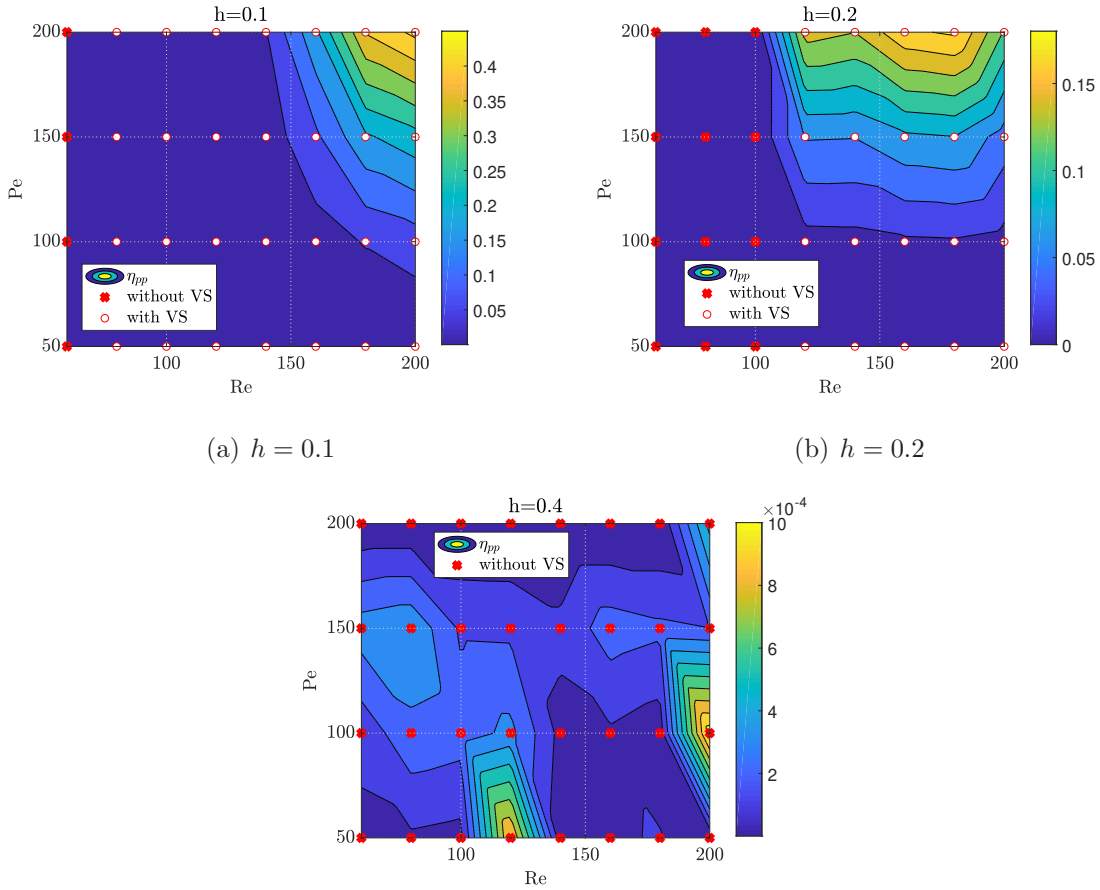

(a) $h = 0.1$

(b) $h = 0.2$

(c) $h = 0.4$

Figure 13: Appearance of Vortex Streets (VS) and peak-to-peak mixing efficiency value as function of Re and Pe for different configurations of the jets: (a) $h = 0.1$; (b) $h = 0.2$; and (c) $h = 0.4$. For $h = 0.1$ and $h = 0.2$ the highest values of η_{pp} are located in test cases with vortex shedding at high Re and Pe. The values of η_{pp} in $h = 0.4$ are too low to extract conclusions, as there is no vortex shedding in any test case configuration.

lead to vortex shedding-based mixing [20].

The impact of the oscillatory motion seen in Figs. 14-16 on the mixing can be inferred by comparison with Figs. 17-22, where results with the smallest and highest Pe, together with the smallest, mid and highest Re are shown. For $Re = 60$, it was shown in Fig. 13 that none of the geometries lead to downstream oscillations, thus this mixing is very dependent on Pe and almost entirely independent on h. When the Re is

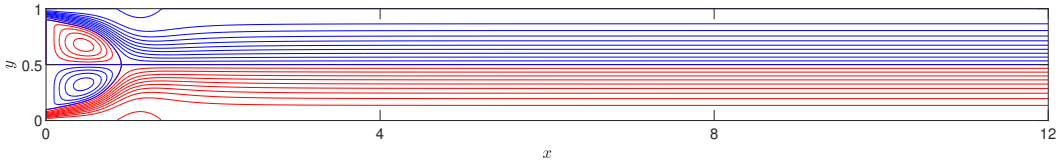

(a) $Re = 60$

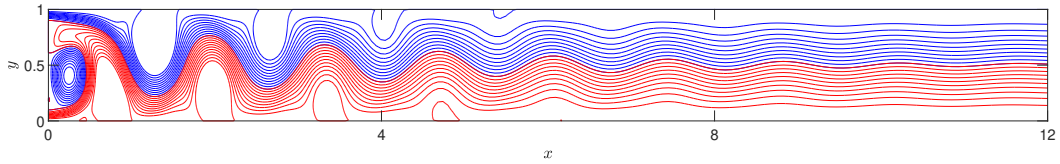

(b) $Re = 120$

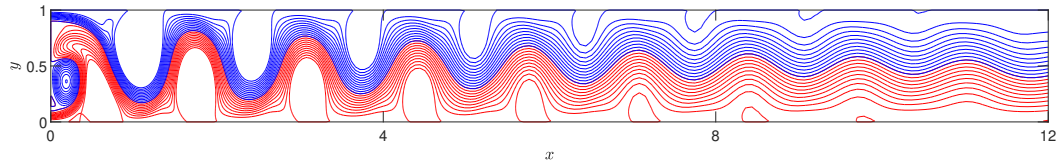

(c) $Re = 200$

Figure 14: Instantaneous streamlines at different Reynolds numbers for the geometry $h = 0.1$. The upper flow is coloured as a blue wall jet, and the lower wall jet is coloured in red. The streamline patterns are different because the higher the Reynolds number, the more intense the oscillatory motion. For $Re = 60$ the flow downstream is steady.

set to an intermediate value of $Re = 120$, $h = 0.1$ and $h = 0.2$ exhibit oscillations, but $h = 0.4$ does not. Nevertheless, if $Pe = 50$, all configurations yield a perfect mixing. However, for the unfavourable case scenario of $Pe = 200$, only the $h = 0.1$ geometry achieves (very quickly in spatial terms) a full mixing, thanks to the intense wavy flow, see Fig. 14(b). The $h = 0.2$ geometry achieves a better mixing than $h = 0.4$, but still very inefficient due to the low intensity oscillations, see Fig. 15(b). For $Re = 200$ the performance of the mixing machine is nearly the same as in $Re = 120$ in terms of mixing efficiency. In principle, it does not seem necessary to increase that much the Reynolds number to improve mixing. This increase in Reynolds number will have an important increase in the required pumping power, as will be shown next.

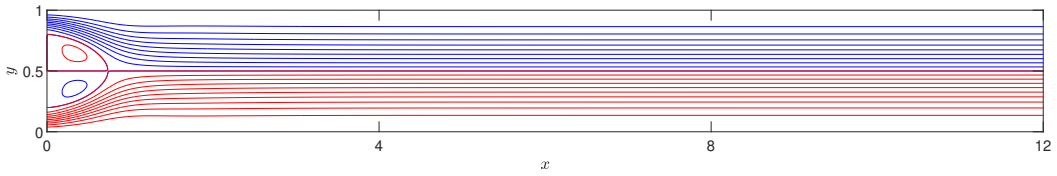

(a) $Re = 60$

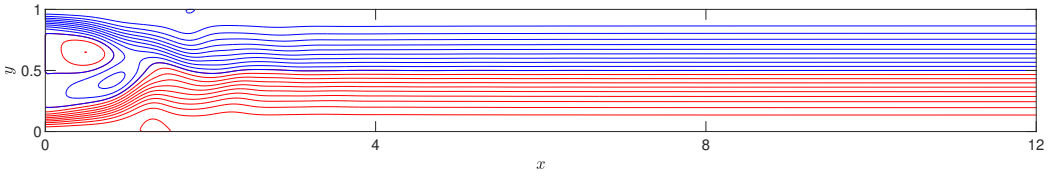

(b) $Re = 120$

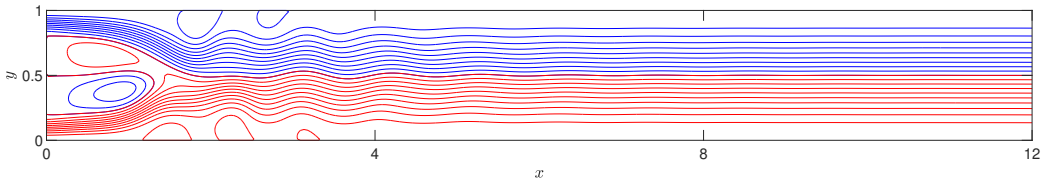

(c) $Re = 200$

Figure 15: Instantaneous streamlines at different Reynolds numbers for the geometry $h = 0.2$. The upper wall jet is coloured in blue, and the lower wall jet is coloured in red. The streamline patterns are different because the higher the Reynolds number, the more intense the oscillatory motion. For $Re = 60$ the flow downstream is steady. For $Re = 120$ the flow downstream is nearly steady.

3.2. Effect on Pressure Drop and Mixing Energy Cost

The effect on pressure drop (and hence on the required pumping power) is depicted in Fig. 23. Due to it is a pure mechanical parameter, it does not depend on Pe. It can be seen that the pressure requirement varies depending on the configuration. For the most efficient mixing geometry, $h = 0.1$, the trend of the pressure drop when increasing the Reynolds number is parabolic-like. The minimum pressure is achieved for a Reynolds number between $Re = 120$ and $Re = 140$. Must be taken into account that the mixing was almost the same for $Re = 120$ and $Re = 200$, so the mixing energy cost will be a good reference for the selection of the ideal geometry and conditions, as will be shown next. For $h = 0.1$ and $h = 0.2$ geometries, the behaviour of the pressure drop is almost nearly decreasing when increasing the Reynolds number. This monotone

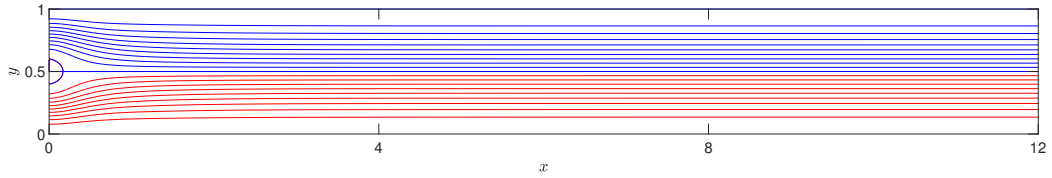

(a) $Re = 60$

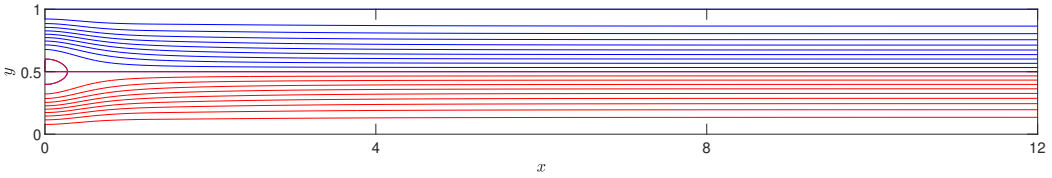

(b) $Re = 120$

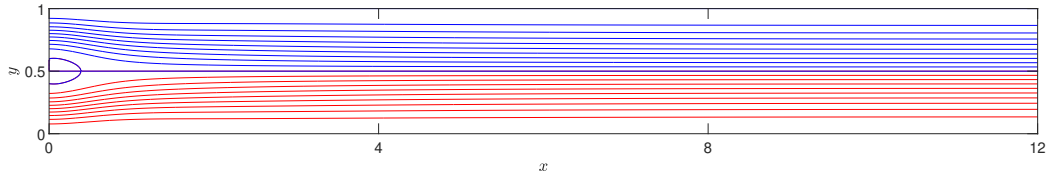

(c) $Re = 200$

Figure 16: Instantaneous streamlines at different Reynolds numbers for the geometry $h = 0.4$. The upper wall jet is coloured in blue, and the lower wall jet is coloured in red. All streamlines reflect steady flows.

decreasing trend is actually parabolic too, but the range of Reynolds numbers analysed for these geometries is not large enough to show the increase expected for higher Re values.

Finally, the mixing energy cost is shown in Fig. 24. It is observed that the trend is actually the same as seen for the pumping power. This is because the results observed for the mixing efficiency were not dramatically affected by the Reynolds number at each geometry as long as there is no change in the oscillatory performance of the geometry when varying Re. That is, for instance for $Re = 60$ in $h = 0.1$ there is a difference with respect to the higher Re tested (see Fig. 12), because at low Re the microdevice has no von Karman streets. From the analysis of Fig. 24 can be concluded that the best option for $h = 0.1$ geometry is a Reynolds number between $Re = 120$ and 140.

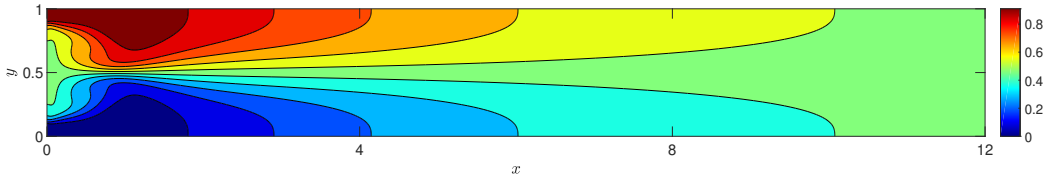

(a) $h = 0.1$

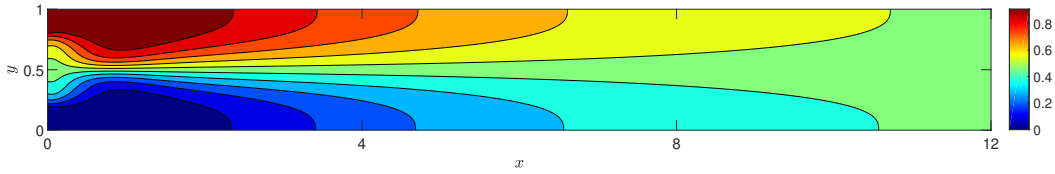

(b) $h = 0.2$

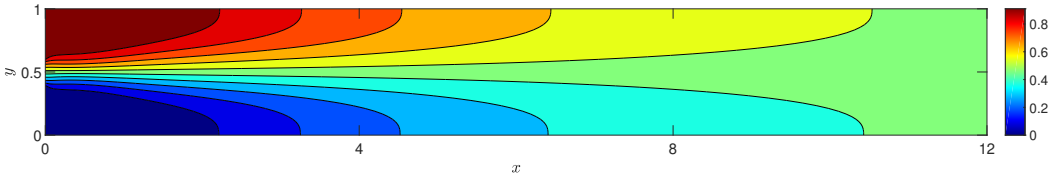

(c) $h = 0.4$

Figure 17: Instantaneous dimensionless mixing quantity contours for $Re = 60$ and $Pe = 50$. The upper wall jet is at $Y = 1$ (dark red), and the lower wall jet is at $Y = 0$ (dark blue). All mixing machines achieved the maximum mixing efficiency before the channel exit ($x = 12$), as $Y = 0.5$. The mixer of geometry $h = 0.1$ achieved a perfect mixing earlier than the other configurations.

In Fig. 12(a) was depicted the mixing efficiency, which was $\sim 100\%$ for this geometry. For $h = 0.2$ and $h = 0.4$, $Re = 200$ seems the most efficient option amongst the tested Reynolds numbers. The configuration with the smaller mixing energy cost is $h = 0.2$ with $Re = 200$. But this configuration yields lower mixing efficiency η than any $h = 0.1$ for the tested $Re > 60$. Obviously, for any configuration, the lower the Pe, the lower the mixing energy cost.

3.3. Effect on the Strouhal Number

Depending on the geometry and Reynolds number, the frequency of the oscillation may vary. As aforementioned, vortex shedding is actually nonexistent for the $h = 0.4$ geometry in the range of $Re \in [60, 200]$. For this reason, in Fig. 25 only the Strouhal

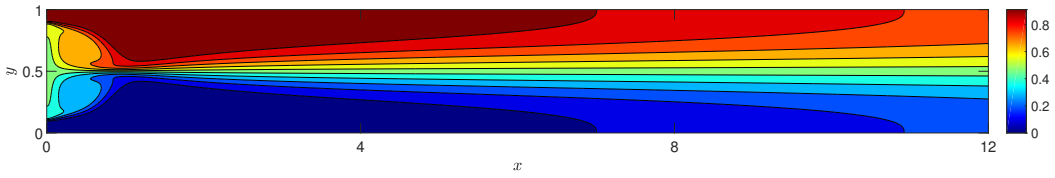

(a) $h = 0.1$

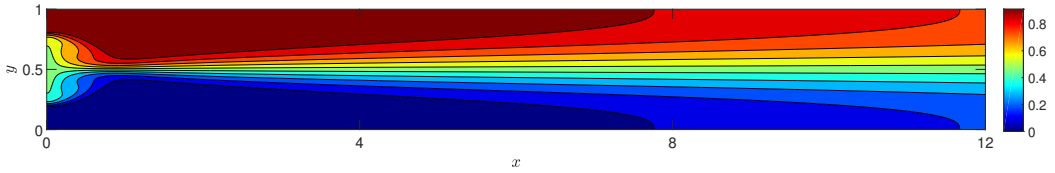

(b) $h = 0.2$

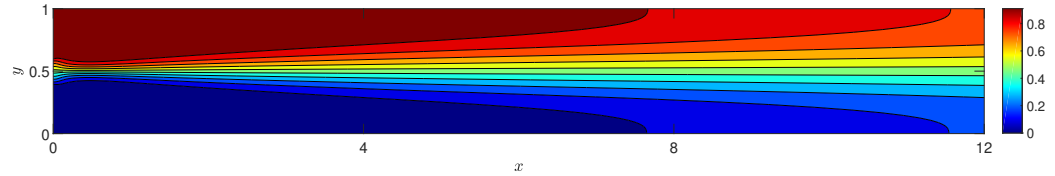

(c) $h = 0.4$

Figure 18: Instantaneous dimensionless mixing quantity contours for $Re = 60$ and $Pe = 200$. The upper wall jet is at $Y = 1$ (dark red), and the lower wall jet is at $Y = 0$ (dark blue). None of the mixing machines achieved the perfect mixing efficiency before the channel exit ($x = 12$), as the profile of Y is not of constant value 0.5 from a certain position x on.

number of the mixing efficiency η for $h = 0.1$ and $h = 0.2$ do appear. It is clear that, from a critical Reynolds number on, the frequency of the oscillation decreases monotonically as the Reynolds number increases, for both $h = 0.1$ and $h = 0.2$. As discussed in [1], the values of the Strouhal number cannot be related to a good or bad mixing in principle. They just provide a dimensionless reference on the frequency of the oscillation, and the amplitude may be either large or small.

3.4. Effect of Channel Length

The length of the channel affects dramatically the mixed outflow. The longer the microchannel, the higher the mixing. This is obvious, since in a long microchannel the flow has more time to mix by the effect of vorticity and diffusion. To take the lengh of

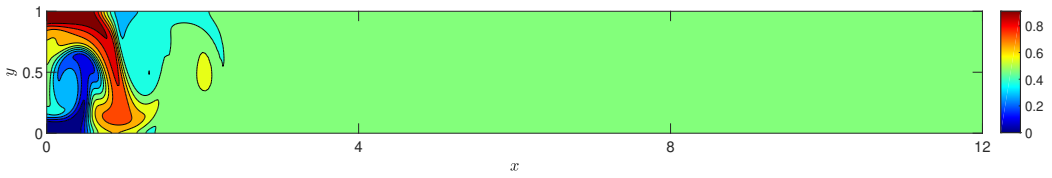

(a) $h = 0.1$

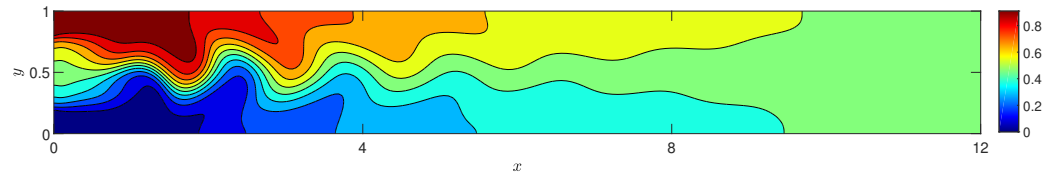

(b) $h = 0.2$

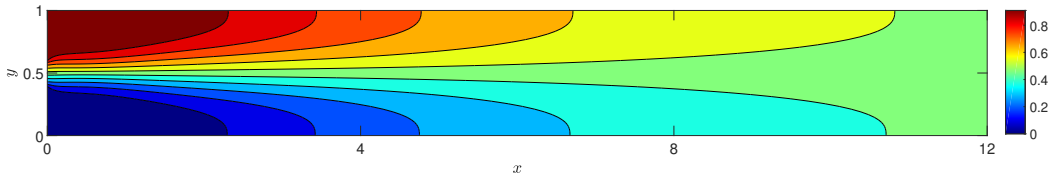

(c) $h = 0.4$

Figure 19: Instantaneous dimensionless mixing quantity contours for $Re = 120$ and $Pe = 50$. The upper wall jet is at $Y = 1$ (dark red), and the lower wall jet is at $Y = 0$ (dark blue). All mixing machines achieved the maximum mixing efficiency before the channel exit ($x = 12$), as $Y = 0.5$. The performance of the mixer of geometry $h = 0.1$ stands out, as the perfect mixing is achieved at $x \approx 3$.

the channel into account, the expression given in Equation (14) allows to evaluate the difference in mixing efficiency between two positions. In particular, the difference will be evaluated between the channel outlet and a relevant position of $x = 5$ as:

$$\Delta\eta = \eta_{outlet} - \eta_{x=5}, \tag{24}$$

where η_{outlet} is the mixing efficiency evaluated at the outlet (the η discussed throughout the paper) and $\eta_{x=5}$ is the mixing efficiency at $x = 5$. This quantity $\Delta\eta$ is useful to predict the contribution in mixing of a portion of channel (in this analysis, the microchannel has a total length of 12 units, so we are evaluating the impact of an extra length of 7 units). The results from this evaluation are depicted in Fig. 26. It is very obvious that the $h = 0.1$ geometry exhibits the lowest impact on mixing efficiency

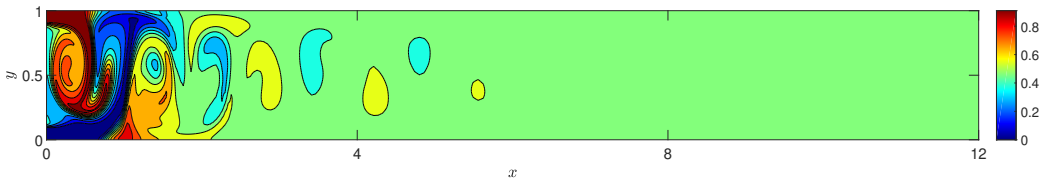

(a) $h = 0.1$

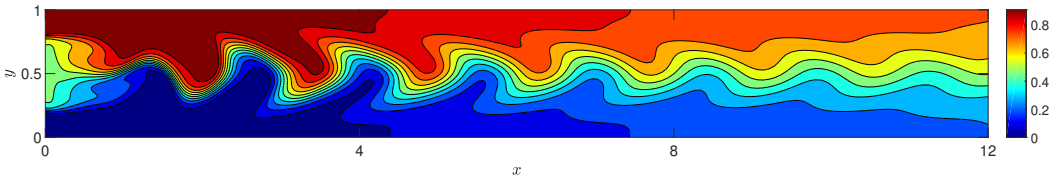

(b) $h = 0.2$

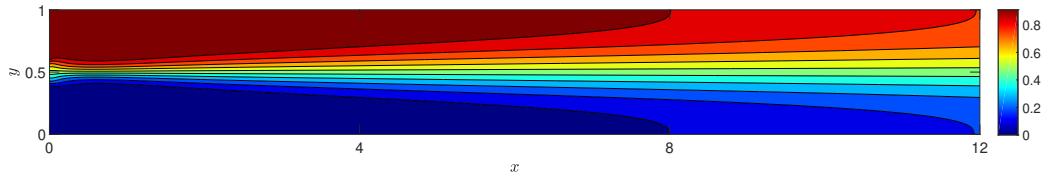

(c) $h = 0.4$

Figure 20: Instantaneous dimensionless mixing quantity contours for $Re = 120$ and $Pe = 200$. The upper wall jet is at $Y = 1$ (dark red), and the lower wall jet is at $Y = 0$ (dark blue). Only the $h = 0.1$ mixing machine achieved the maximum mixing efficiency before the channel exit (at $x \approx 5.8$). The $h = 0.2$ mixing device achieved an oscillatory state, resulting in a better performance than the $h = 0.4$ one.

when increasing the channel length. Thus a very short channel could have been used, specially for a low Peclet-like number. To understand the contribution to the total mixing efficiency, one can see Fig. 27. In this figure it is shown the mixing achieved at $x = 5$ (blue) and the mixing due to the additional channel length (orange). The sum of these two quantities yields the total mixing η at the outlet. From this figure can be seen that for $h = 0.2$ and $h = 0.4$, $\Delta\eta$ is nearly constant. However, the $h = 0.1$ geometry provides nearly the 100% of the mixing efficiency at $x = 5$ for $Re = 200$, which is a case scenario of intense downstream oscillations. Thus, for this geometry a very short channel would be enough to get a highly efficient mixing performance. This would also reduce the pressure drop notably.

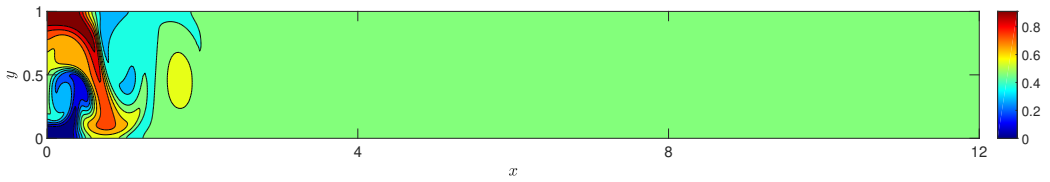

(a) $h = 0.1$

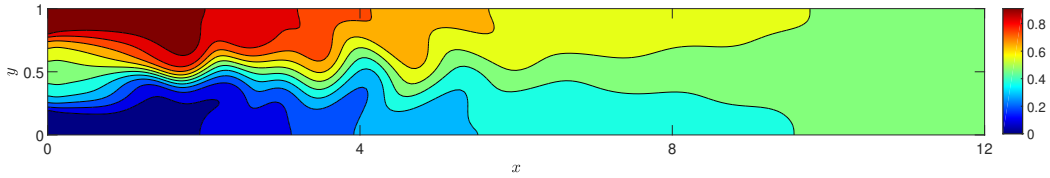

(b) $h = 0.2$

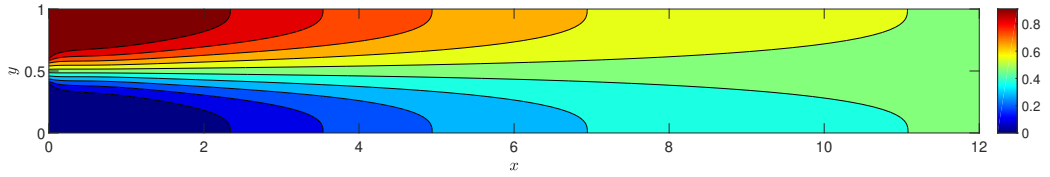

(c) $h = 0.4$

Figure 21: Instantaneous dimensionless mixing quantity contours for $Re = 200$ and $Pe = 50$. The upper wall jet is at $Y = 1$ (dark red), and the lower wall jet is at $Y = 0$ (dark blue). All mixing machines achieved the maximum mixing efficiency before the channel exit ($x = 12$), as $Y = 0.5$. The mixer of geometry $h = 0.1$ achieved a perfect mixing much earlier than the other configurations.

4. Conclusions

This paper has presented the novel use of two parallel wall jets as passive elements to enhance mixing mechanically by promoting flow oscillations in heat/mass exchangers. The parallel wall jets are constrained in a microchannel, which can be a device with potential use as scalable mixing device. Different channel ratios (wall jet widths) h have been tested numerically with a verified&validated CFD code based on non-uniform finite difference approximation.

From the analysis carried out in the paper, can be concluded that a small channel ratio of $h = 0.1$ is more beneficial to enhance mixing. The reason is that intense flow oscillations take place, which enhances mixing notably. Full mixing in this configuration

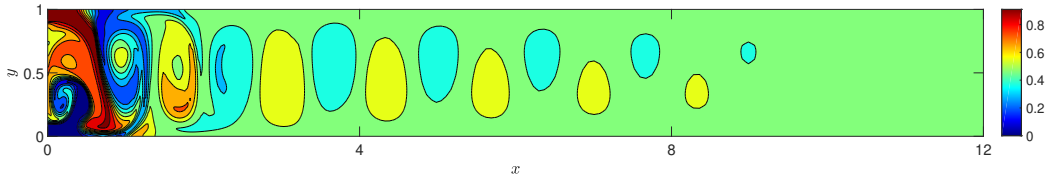

(a) $h = 0.1$

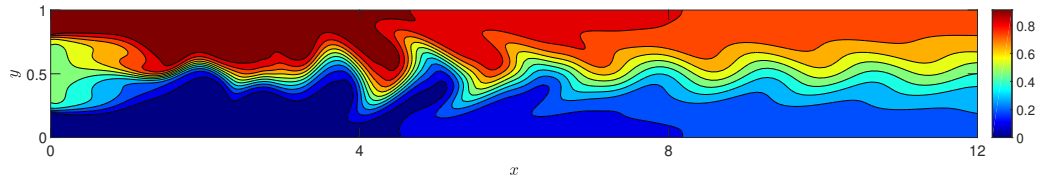

(b) $h = 0.2$

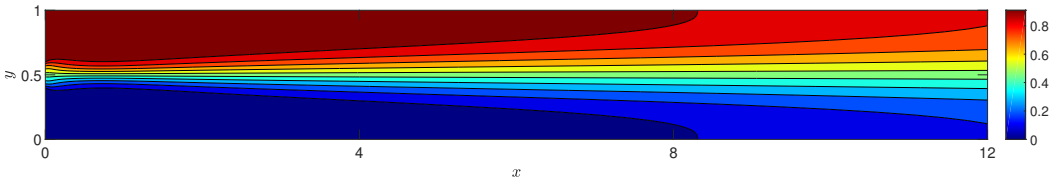

(c) $h = 0.4$

Figure 22: Instantaneous dimensionless mixing quantity contours for $Re = 200$ and $Pe = 200$. The upper wall jet is at $Y = 1$ (dark red), and the lower wall jet is at $Y = 0$ (dark blue). Only the $h = 0.1$ mixing machine achieved the maximum mixing efficiency before the channel exit (at $x \approx 9$). The $h = 0.2$ mixing device achieved an oscillatory state, resulting in a better performance than the $h = 0.4$ one.

is happening quite early, which allows to shorten the channel length considerably and require a lower pumping power consumption. The tested $h = 0.2$ and $h = 0.4$ geometries yielded unsatisfactory mixing efficiency results in contrast to $h = 0.1$. The reason behind is the well-known fact that both the Reynolds number and geometry play an important role in boosting or damping the flow oscillations. Actually, to achieve a non-steady simulation for $h = 0.4$ one has to increase the Reynolds number above $Re = 400$. For the most promising configuration, $h = 0.1$, it has been observed also that the pumping power achieved its minimum between $Re = 120$ and 140. Since the mixing efficiency was nearly the same for these Reynolds numbers and $Re = 200$, an optimal performance would be within that range. Upon a channel length analysis, it

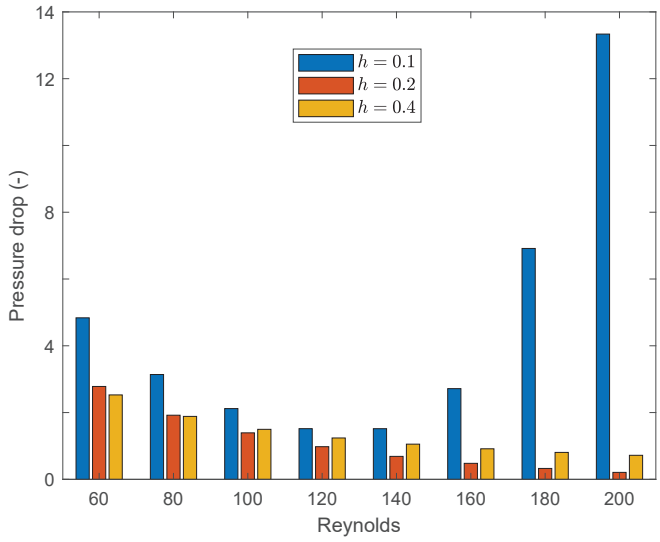

Figure 23: Pressure drop for each configuration as function of Re for different configurations of the jets.

has been also noticed that for fluids with a Peclet-like number between 50 and 200, and regimes between Reynolds 120 and 140, the channel length can be shortened at least to a length of 5 units and keep nearly the same outlet mixing efficiency. This reduces the pressure drop, and thence, the mixing efficiency cost.

Acknowledgements

The authors acknowledge the financial support from the UMA18-FEDERJA-184 and The Andalusian Research, Development and Innovation Plan (PAIDI - Junta de Andalucia) fundings for the postdoctoral grant of the first author.

References

[1] Francisco-Javier Granados-Ortiz and Joaquín Ortega-Casanova. Mechanical characterisation and analysis of a passive micro heat exchanger. *Micromachines*, 11(7):668, 2020.

[2] Teruo Suzuki and Yoshihito Sakurai. Effect of hydrogen rich gas and gasoline mixed combustion on spark ignition engine. Technical report, SAE Technical Paper, 2006.

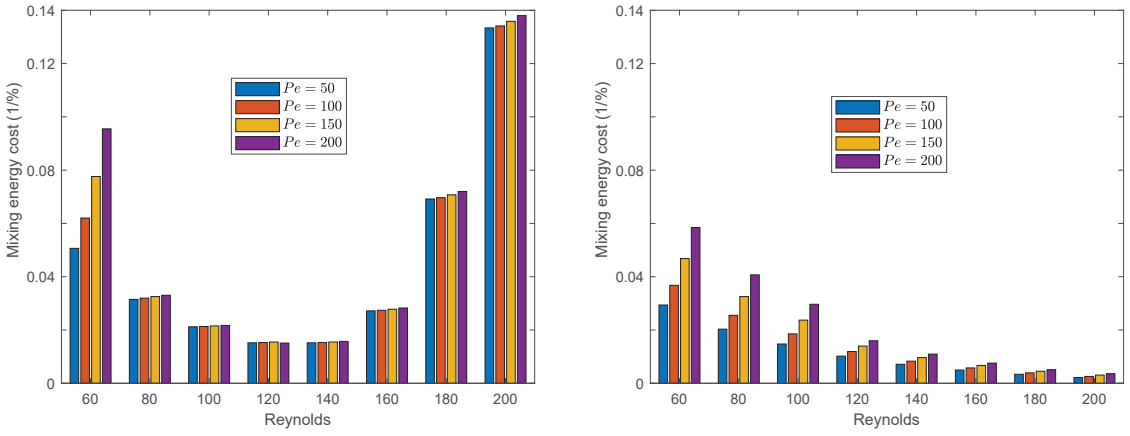

(a) $h = 0.1$ (b) $h = 0.2$

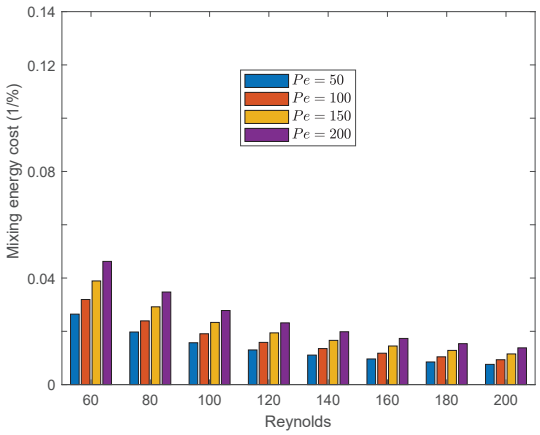

(c) $h = 0.4$

Figure 24: Mixing energy cost as function of Re and Pe for different configurations of the jets: (a) $h = 0.1$; (b) $h = 0.2$; and (c) $h = 0.4$.

[3] Ashish Nedungadi and Mark J Lewis. Numerical study of fuel mixing enhancement using an oblique shock/vortex interaction. *Journal of Propulsion and Power*, 16(6):946–955, 2000.

[4] Masaya Kakuta, Fiona G Bessoth, and Andreas Manz. Microfabricated devices for fluid mixing and their application for chemical synthesis. *The Chemical Record*, 1(5):395–405, 2001.

[5] Jiandong Wu, Meili Dong, Claudio Rigatto, Yong Liu, and Francis Lin. Lab-On-

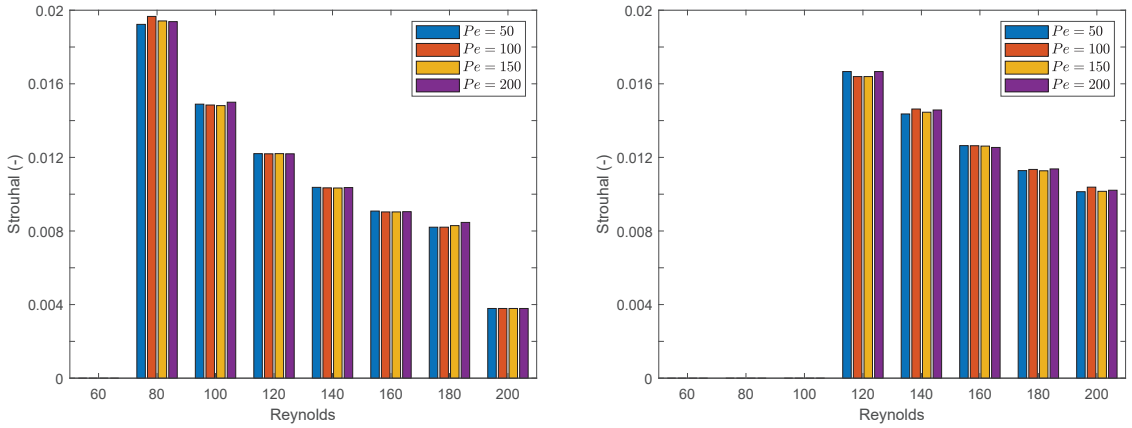

(a) $h = 0.1$ (b) $h = 0.2$

Figure 25: Strouhal number of the mixing efficiency η as function of Re and Pe for different configurations of the jets: (a) $h = 0.1$; and (b) $h = 0.2$. The solution for $h = 0.4$ is steady.

669 Chip technology for chronic disease diagnosis. *Nature Partner Journal - Digital*
670 *Medicine*, 1(1):1–11, 2018.

671 [6] Volker Hessel, Holger Löwe, and Friedhelm Schönfeld. Micromixers—a review on
672 passive and active mixing principles. *Chemical Engineering Science*, 60(8-9):2479–
673 2501, 2005.

674 [7] Nikita Kavokine, Roland R Netz, and Lydéric Bocquet. Fluids at the nanoscale:
675 From continuum to subcontinuum transport. *Annual Review of Fluid Mechanics*,
676 53:377–410, 2021.

677 [8] Blaž Likozar, Andrej Pohar, and Janez Levec. Transesterification of oil to biodiesel
678 in a continuous tubular reactor with static mixers: Modelling reaction kinetics,
679 mass transfer, scale-up and optimization considering fatty acid composition. *Fuel*
680 *Processing Technology*, 142:326–336, 2016.

681 [9] Thierry Meyer. Scale-up of polymerization process: a practical example. *Organic*
682 *process research & development*, 7(3):297–302, 2003.

683 [10] Tae-Seok Lee and Peter Witting. Computational fluid dynamics (CFD) analysis

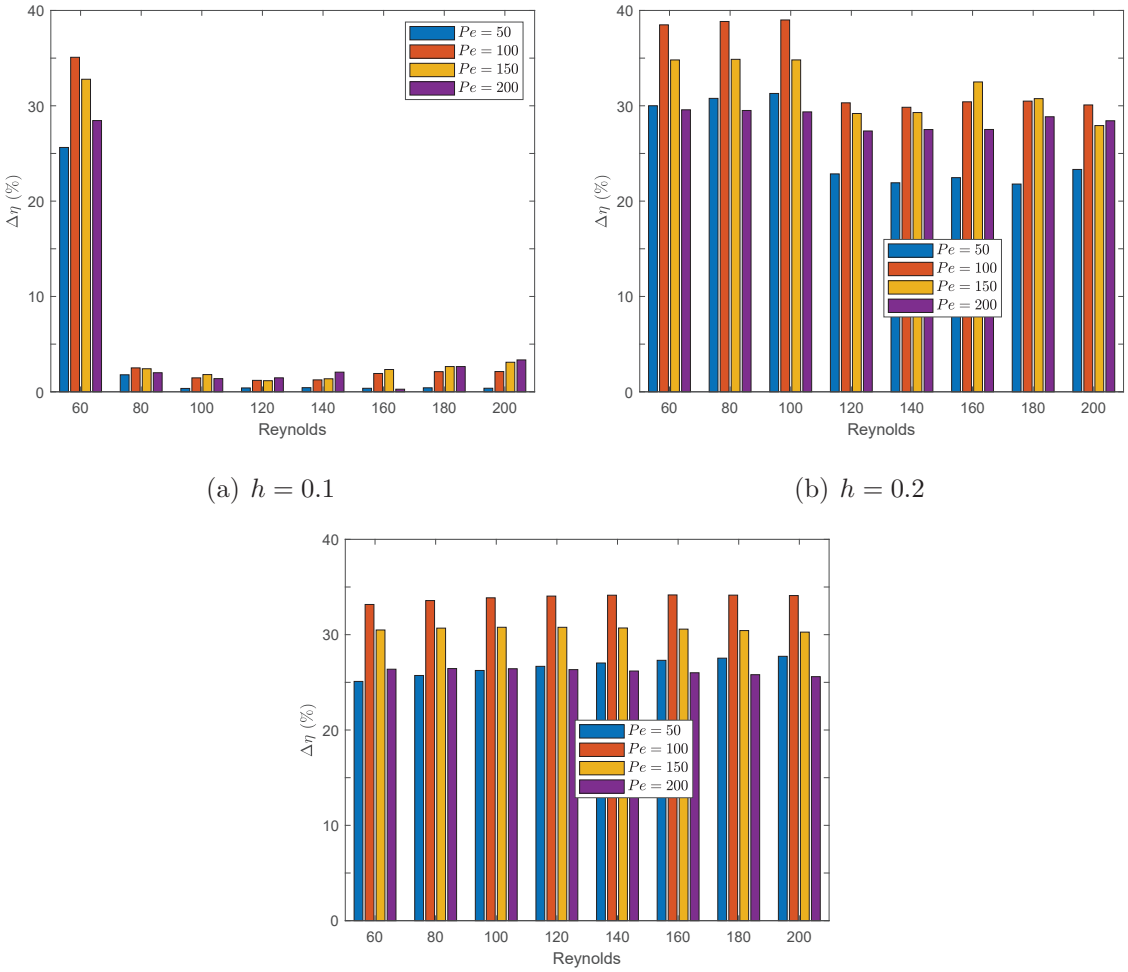

(a) $h = 0.1$

(b) $h = 0.2$

(c) $h = 0.4$

Figure 26: Instantaneous efficiency difference $\Delta\eta$ as function of Re and Pe for different configurations of the jets: (a) $h = 0.1$; and (b) $h = 0.2$; and (c) $h = 0.4$.

for off-gas mixing and ventilation inside carbonization furnace during PAN-based carbon fiber manufacturing. In *SAMPE 2016 Conference Proceeding*, 2016.

[11] Bin Xu, Teck Neng Wong, Nam-Trung Nguyen, Zhizhao Che, and John Chee Kiong Chai. Thermal mixing of two miscible fluids in a T-shaped microchannel. *Biomicrofluidics*, 4(4):044102, 2010.

[12] Xueye Chen and Jienan Shen. Simulation and experimental analysis of a SAR micromixer with F-shape mixing units. *Analytical Methods*, 9(12):1885–1890, 2017.

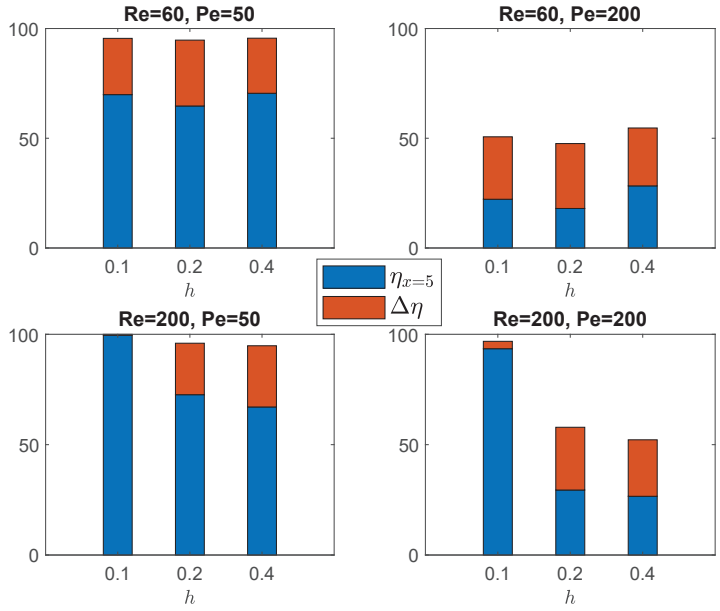

Figure 27: Instantaneous outlet mixing efficiency ($\eta_{x=5} + \Delta\eta$) and efficiency difference $\Delta\eta$ for different extreme combinations of Re and Pe. Both the mixing efficiency and efficiency difference are provided in % units.

[13] Imran Shah, Soo Wan Kim, Kyunghwan Kim, Yang Hoi Doh, and Kyung Hyun Choi. Experimental and numerical analysis of Y-shaped split and recombination micro-mixer with different mixing units. *Chemical Engineering Journal*, 358:691–706, 2019.

[14] Nassim Ait Mouheb, Daniéll Malsch, Agnès Montillet, Camille Solliec, and Thomas Henkel. Numerical and experimental investigations of mixing in T-shaped and cross-shaped micromixers. *Chemical Engineering Science*, 68(1):278–289, 2012.

[15] Yong Kweon Suh and Sangmo Kang. A review on mixing in microfluidics. *Micromachines*, 1(3):82–111, 2010.

[16] J Ortega-Casanova. Application of CFD on the optimization by response surface methodology of a micromixing unit and its use as a chemical microreactor. *Chemical Engineering and Processing: Process Intensification*, 117:18–26, 2017.

[17] Naas Toufik Tayeb, Kouadri Amar, Khelladi Sofiane, and Laib Lakhdar. Thermal

mixing performances of shear-thinning non-newtonian fluids inside two-layer crossing channels micromixer using entropy generation method: Comparative study. *Chemical Engineering and Processing-Process Intensification*, 156:108096, 2020.

[18] Li-Yu Tseng, An-Shik Yang, Chun-Ying Lee, and Chang-Yu Hsieh. CFD-based optimization of a diamond-obstacles inserted micromixer with boundary protrusions. *Engineering Applications of Computational Fluid Mechanics*, 5(2):210–222, 2011.

[19] J Ortega-Casanova. On the onset of vortex shedding from 2D confined rectangular cylinders having different aspect ratios: Application to promote mixing fluids. *Chemical Engineering and Processing-Process Intensification*, 120:81–92, 2017.

[20] Francisco-Javier Granados-Ortiz, Marina Garcia-Cardosa, and J. Ortega-Casanova. Predicting the behaviour of a vortex shedding-based passive mechanical micro heat exchanger. In *Journal of Physics: Conference series*, 2020.

[21] Aditya Desai, Sanchit Mittal, and Sanjay Mittal. Experimental investigation of vortex shedding past a circular cylinder in the high subcritical regime. *Physics of Fluids*, 32(1):014105, 2020.

[22] MR Islam and A Mohany. Vortex shedding characteristics in the wake of circular finned cylinders. *Physics of Fluids*, 32(4):045113, 2020.

[23] Tingting Tang, Peng Yu, Xiaowen Shan, Jianhui Li, and Shimin Yu. On the transition behavior of laminar flow through and around a multi-cylinder array. *Physics of Fluids*, 32(1):013601, 2020.

[24] Vedant Kumar, Hemanshul Garg, Gaurav Sharma, and Rajneesh Bhardwaj. Harnessing flow-induced vibration of a D-section cylinder for convective heat transfer augmentation in laminar channel flow. *Physics of Fluids*, 32(8):083603, 2020.

[25] Wan Sun, Soohwan Jo, and Jongwon Seok. Development of the optimal bluff body for wind energy harvesting using the synergetic effect of coupled vortex induced

730 vibration and galloping phenomena. *International Journal of Mechanical Sciences*,
731 156:435–445, 2019.

732 [26] Zhen Li, Chuanjin Lan, Laibing Jia, and Yanbao Ma. Ground effects on separated
733 laminar flows past an inclined flat plate. *Theoretical and Computational Fluid*
734 *Dynamics*, 31(2):127–136, 2017.

735 [27] Xikun Wang, Jiaqi Chen, Bo Zhou, Yajie Li, and Qingjiang Xiang. Experimental
736 investigation of flow past a confined bluff body: Effects of body shape, blockage
737 ratio and reynolds number. *Ocean Engineering*, 220:108412, 2021.

738 [28] F-J Granados-Ortiz and J Ortega-Casanova. Machine Learning-Aided Design Op-
739 timisation of a mechanical micromixer. *Physics of Fluids*, 2021. (minor revisions
740 sent).

741 [29] A Venugopal, Amit Agrawal, and SV Prabhu. Vortex dynamics of a trapezoidal
742 bluff body placed inside a circular pipe. *Journal of Turbulence*, 19(1):1–24, 2018.

743 [30] Apoorv Vyas, Biswajit Mishra, and Atul Srivastava. Investigation of the effect of
744 blockage ratio on flow and heat transfer in the wake region of a cylinder embedded
745 in a channel using whole field dynamic measurements. *International Journal of*
746 *Thermal Sciences*, 153:106322, 2020.

747 [31] Marco Carini, Christophe Airiau, Antoine Debien, Olivier Léon, and JO Pralits.
748 Global stability and control of the confined turbulent flow past a thick flat plate.
749 *Physics of Fluids*, 29(2):024102, 2017.

750 [32] Rajendran Senthilkumar, Premalatha Vasudevan, and Sethuramalingam Prabhu.
751 Neural network and multi-objective optimization of confined flow characteristics
752 on circular cylinder in standing double vortex region. *Neural Computing and Ap-*
753 *plications*, 33(4):1379–1398, 2021.

[33] Wang Han, Arne Scholtissek, Felix Dietzsch, and Christian Hasse. Thermal and chemical effects of differential diffusion in turbulent non-premixed H2 flames. *Proceedings of the Combustion Institute*, 38(2):2627–2634, 2021.

[34] F-J Granados-Ortiz and J Ortega-Casanova. Quantifying & analysing mixed aleatoric and structural uncertainty in complex turbulent flow simulations. *International Journal of Mechanical Sciences*, 188:105953, 2020.

[35] Luca Antiga and David A Steinman. Rethinking turbulence in blood. *Biorheology*, 46(2):77–81, 2009.

[36] Centers for Disease Control and Prevention. Pfizer-BioNTech COVID-19 Vaccine. `https://www.cdc.gov/vaccines/covid-19/info-by-product/pfizer/index.html`, 2021. [Online; accessed 08-June-2021].

[37] Centers for Disease Control and Prevention. Manual for Pfizer-BioNTech COVID-19 Vaccine. `https://www.cdc.gov/vaccines/covid-19/info-by-product/pfizer/downloads/prep-and-a` 2021. [Online; accessed 08-June-2021].

[38] Ian Rafferty and Deborah Kaminski. Non-dimensionalization and mixing quantification of laminar twin semi-confined jets. *International journal of heat and fluid flow*, 48:15–23, 2014.

[39] A Nahum and A Seifert. On the application of confined twin-jet instability to micro-mixing enhancement. *Physics of Fluids*, 18(6):064107, 2006.

[40] M Mosavati, R Balachandar, and RM Barron. Characteristics of self-oscillating twin jets. *Physics of Fluids*, 33(3):035129, 2021.

[41] Mehmet N Tomac and James W Gregory. Oscillation characteristics of mutually impinging dual jets in a mixing chamber. *Physics of Fluids*, 30(11):117102, 2018.

[42] XK Wang and SK Tan. Experimental investigation of the interaction between a plane wall jet and a parallel offset jet. *Experiments in Fluids*, 42(4):551–562, 2007.

[43] Li Zhiwei, Huai Wenxin, and Yang Zhonghua. Interaction between wall jet and offset jet with different velocity and offset ratio. *Procedia Engineering*, 28:49–54, 2012.

[44] Amitesh Kumar. Mean flow characteristics of a turbulent dual jet consisting of a plane wall jet and a parallel offset jet. *Computers & Fluids*, 114:48–65, 2015.

[45] Mohammad Mosaddeghi. Two dimensional simulation of laminar flow by three-jet in a semi-confined space. *Nonlinear Engineering*, 9(1):111–117, 2020.

[46] Yasin Varol, Besir Kok, Hüseyin Ayhan, and Hakan F Oztop. Experimental study and large eddy simulation of thermal mixing phenomena of a parallel jet with perforated obstacles. *International Journal of Thermal Sciences*, 111:1–17, 2017.

[47] Besir Kok, Yasin Varol, Hüseyin Ayhan, and Hakan F Oztop. Experimental and les simulation of thermal mixing behavior of a twin-jet flow with sequential cylindrical obstacles. *International Communications in Heat and Mass Transfer*, 114:104576, 2020.

[48] Besir Kok, Murat Uyar, Yasin Varol, Ahmet Koca, and Hakan F Oztop. Analyzing of thermal mixing phenomena in a rectangular channel with twin jets by using artificial neural network. *Nuclear Engineering and Design*, 265:554–565, 2013.

[49] E Sanmiguel-Rojas, J Ortega-Casanova, C Del Pino, and R Fernandez-Feria. A cartesian grid finite-difference method for 2D incompressible viscous flows in irregular geometries. *Journal of Computational Physics*, 204(1):302–318, 2005.

[50] F-J Granados-Ortiz, L Rodriguez-Tembleque, and J Ortega-Casanova. Vortex breakdown mechanics of a laminar confined swirling flow with large expansion ratio using a non-uniform finite difference approximation. *Part C: Journal of Mechanical Engineering Science*, 2021. (In press).

[51] E Sanmiguel-Rojas and R Fernandez-Feria. Nonlinear instabilities in a vertical pipe flow discharging from a cylindrical container. *Physics of Fluids*, 18(2):024101, 2006.

[52] Virginie Mengeaud, Jacques Josserand, and Hubert H Girault. Mixing processes in a zigzag microchannel: finite element simulations and optical study. *Analytical chemistry*, 74(16):4279–4286, 2002.

[53] A Arun Govind Neelan and Manoj T Nair. Hybrid Finite Difference-Finite Volume Schemes on non-uniform grid. In *Applications of Fluid Dynamics*, pages 329–340. Springer, 2018.

[54] Simon Heru Prassetyo and Marte Gutierrez. High-order ADE scheme for solving the fluid diffusion equation in non-uniform grids and its application in coupled hydro-mechanical simulation. *International Journal for Numerical and Analytical Methods in Geomechanics*, 42(16):1976–2000, 2018.

[55] Simon Heru Prassetyo and Marte Gutierrez. Explicit high-order ADE solutions for fluid flow in the coupled biot equations. In *Poromechanics VI*, pages 215–222. 2017.

[56] Joaquim Peiró and Spencer Sherwin. Finite difference, finite element and finite volume methods for partial differential equations. In *Handbook of materials modeling*, pages 2415–2446. Springer, 2005.

[57] Nick Pepper, Francesco Montomoli, and Sanjiv Sharma. Multiscale uncertainty quantification with arbitrary polynomial chaos. *Computer Methods in Applied Mechanics and Engineering*, 357:112571, 2019.

[58] Jeongeun Son and Yuncheng Du. Comparison of intrusive and nonintrusive polynomial chaos expansion-based approaches for high dimensional parametric uncertainty quantification and propagation. *Computers & Chemical Engineering*, 134:106685, 2020.

[59] Banamali Dalai and Manas Kumar Laha. Numerical solution of steady incompressible flow in a lid-driven cavity using Alternating Direction Implicit method. In *Recent Advances in Theoretical, Applied, Computational and Experimental Mechanics*, pages 353–364. Springer, 2020.

[60] Shobha Bagai, Manoj Kumar, and Arvind Patel. The four-sided lid driven square cavity using stream function-vorticity formulation. *Journal of Applied Mathematics and Computational Mechanics*, 19(2):17–30, 2020.

[61] Zhigang Wu and Nam-Trung Nguyen. Convective–diffusive transport in parallel lamination micromixers. *Microfluidics and Nanofluidics*, 1(3):208–217, 2005.

[62] J Ortega-Casanova and C-H Lai. CFD study about the effect of using multiple inlets on the efficiency of a micromixer. Assessment of the optimal inlet configuration working as a microreactor. *Chemical Engineering and Processing-Process Intensification*, 125:163–172, 2018.

[63] S Abdallah. Numerical solutions for the pressure Poisson equation with neumann boundary conditions using a non-staggered grid, I. *Journal of computational physics*, 70(1):182–192, 1987.

[64] Quanbing Luo, Ting Ren, and Dong Liang. Discretized pressure Poisson algorithm for the steady incompressible flow on a nonstaggered grid. *Numerical Heat Transfer, Part B: Fundamentals*, 71(6):549–559, 2017.

[65] Sourav Sarkar, KK Singh, V Shankar, and KT Shenoy. Numerical simulation of mixing at 1–1 and 1–2 microfluidic junctions. *Chemical Engineering and Processing: Process Intensification*, 85:227–240, 2014.

[66] J Ortega-Casanova and C-H Lai. CFD study on laminar mixing at a very low reynolds number by pitching and heaving a square cylinder. *Computers & Fluids*, 168:318–327, 2018.

[67] Yuhang Wang, Saman A Aryana, Frederico Furtado, and Victor Ginting. Analysis of nonequilibrium effects and flow instability in immiscible two-phase flow in porous media. *Advances in Water Resources*, 122:291–303, 2018.

[68] Patrick J Roache. Perspective: a method for uniform reporting of grid refinement studies. 1994.

[69] Fotis Sotiropoulos and S Abdallah. Coupled fully implicit solution procedure for the steady incompressible Navier-Stokes equations. *Journal of Computational Physics*, 87(2):328–348, 1990.

[70] Jeffrey P Van Doormaal and George D Raithby. Enhancements of the simple method for predicting incompressible fluid flows. *Numerical heat transfer*, 7(2):147–163, 1984.

Appendix A. Streamfunction-vorticity boundary conditions.

The corresponding boundary conditions to solve Equations (5)–(6) are:

Inlet ($x = 0$). At the inlet, the flow fully developed (parabolic). This means that the components of the velocity are known:

Primitive variables: $\vec{v}^{in} = (u^{in}, 0, 0)$;

$$u^{in} = \begin{cases} \dfrac{6}{(1+\alpha)h^3} y(h-y), & 0 \le y \le h, \\ \\ \dfrac{6\alpha}{(1+\alpha)(\beta h)^3}(y-h')(1-y), & h' \le y \le 1. \end{cases} \tag{A.1}$$

Non-primitive variables:

$$\psi^{in} = \int_0^y u^{in} dy,\ \omega^{in} = -u_y^{in} + v_x = -u_y^{in} + \psi_{xx_0}. \tag{A.2}$$

The subscript xx_0 (or else yy_0) means a finite difference approximation of the second derivative with null first derivative because of $\psi_x = 0 = v$ (or $\psi_y = 0 = u$).

Solid wall ($y =$ constant). At horizontal walls, the components of the velocity are known:

Primitive variables: $\vec{v}^{wall} = (0, 0, 0)$;

Non-primitive variables:

$$\psi^{wall} = \text{constant},\ \omega^{wall} = -u_y + v_x = -u_y = -\psi_{yy_0} \tag{A.3}$$

since on the wall $v = v_x = 0$ and $u = \psi_y = 0$.

Solid wall ($x =$ constant). At vertical walls, the components of the velocity are known:

Primitive variables: $\vec{v}^{wall} = (0, 0, 0)$;

Non-primitive variables:

$$\psi^{wall} = \text{constant},\ \omega^{wall} = -u_y + v_x = v_x = \psi_{xx_0}, \tag{A.4}$$

since on the wall $u = u_y = 0$ and $v = \psi_x = 0$.

Outlet ($x =$ constant). At the outlet, outflow conditions in terms of null derivatives are imposed, which allows to obtain the value at the boundary in terms of upstream known values:

Primitive variables: $v_x = 0$;

Non-primitive variables:

$$\psi_{xx} = 0 = \omega_{xx}. \tag{A.5}$$

Appendix B. Mass fraction/Temperature boundary conditions.

To solve Equation (7) one has to take into account the boundary conditions that, on the different boundaries, are given by:

Inlet ($x = 0$).

$$0 \leq y \leq h : \ Y^{in} = 0; \tag{B.1}$$

$$H - h \leq y \leq H : \ Y^{in} = 1; \tag{B.2}$$

Solid wall ($y =$ constant):

$$Y_x^{wall} = 0; \tag{B.3}$$

Solid wall ($x =$ constant):

$$Y_y^{wall} = 0; \tag{B.4}$$

Outlet ($x =$ constant): Null Newmann condition at the outlet:

$$Y_x = 0. \tag{B.5}$$

Appendix C. Pressure boundary conditions

The boundary conditions to solve Equation (9) can be derived from the momentum equation. They can be written as [69]:

$$\vec{v}_t + (\vec{v} \cdot \nabla)\vec{v} = -\nabla p - \frac{1}{Re}\nabla \wedge \vec{\Omega}, \tag{C.1}$$

from which the corresponding normal gradient to a boundary can be known. Therefore, on the different boundaries one can obtain:

Inlet/Outlet ($x =$ constant).

$$p_x = -\frac{1}{Re}\omega_y - (uu_x + vu_y) - u_t; \tag{C.2}$$

Solid wall ($y =$ constant).

$$p_y = \frac{1}{Re}\omega_x; \tag{C.3}$$

Solid wall ($x =$ constant).

$$p_x = -\frac{1}{Re}\omega_y; \tag{C.4}$$

Finally, to be able to solve Equation (9) and in order to obtain a unique pressure distribution, a reference pressure value must be given at an arbitrary point [70]. In particular, an arbitrary value of 5 units has been set at the middle of the domain.